Late Cretaceous to late Eocene exhumation in the Nima area, central Tibet: Implications for development of low relief topography of the Tibetan Plateau

Weiwei Xue [1], Yani Najman [2], Xiumian Hu [1*], Cristina Persano [3], Finlay M. Stuart [4], Wei Li [1], Anlin Ma [1], Ying Wang [5]

(1) School of Earth Sciences and Engineering, Nanjing University, Nanjing, 210063, China; (2) Lancaster Environment Centre, Lancaster University, Lancaster, LA1 4YK, UK; (3) School of Geographical and Earth Sciences, College of Science and Engineering, University of Glasgow, Glasgow G12 8QQ, UK; (4) Scottish Universities Environmental Research Centre, East Kilbride G75 0QF, UK; (5) State Key Laboratory of Earthquake Dynamics, Institute of Geology, China Earthquake Administration, Beijing, 100029, China

*E-mail: huxm@nju.edu.cn

Key Points:

- Low temperature thermochronology records moderate exhumation of the Nima area from 70 to 30 Ma, after which time exhumation slowed.
- Generation of local thrust-related relief over the period of 70-30 Ma may have played a role in the development of internal drainage by 30 Ma.
- The transition to tectonic quiescence and/or the establishment of internal drainage may have led to the development of low relief topography.

Abstract

Much of the interior of the Tibetan Plateau is characterized by internal drainage, low relief topography and high altitude. How and when this landscape formed is controversial. In this study, we use new zircon U-Pb data and low temperature thermochronological data (apatite and zircon (U-Th/He), apatite fission track (AFT)) from the Late Cretaceous to Cenozoic Nima basin sedimentary rocks and Xiabie granite in the adjacent Muggar Thrust hanging wall (part of the regional Shiquanhe-Gaize-Amdo thrust system), to determine the palaeodrainage and timing of exhumation in the region. Individual AHe and ZHe cooling ages range from 9 to 60 Ma and 58-118 Ma, and the AFT ages range from 30-90 Ma. The thermal history derived from the Northern Nima Basin sediments and Xiabie granite require a period of exhumation between 70 and 40 Ma in the thrust fault hanging wall, and 40 to 30 Ma in the Nima Basin. Across the region this event was followed by low rates of exhumation and the deposition of locally-sourced sediment, lacustrine and evaporitic deposits that are indicative of an internal drainage system. We suggest that the exhumation event is associated with development of thrust-elevated relief that may have disrupted the drainage network favouring the development of an endorheic system. This system, sediment accumulation and/or post-30 Ma tectonic quiescence led to the generation of low relief topography.

Plain Language Summary

The Tibetan Plateau is the highest altitude low topographic relief region on Earth. There is no consensus on how the flat topography formed. Low-temperature thermochronology is widely used to establish the time of exhumation of rocks to the Earth's surface. In this study, we found that the rocks in the Nima area of the central Tibetan Plateau experienced moderate exhumation from Late Cretaceous to early Oligocene (70-30 Ma), after which time the exhumation rate slowed. Such low rates imply slowing of local tectonic activity. The Sedimentology and Stratigraphy of the basin indicate that an internal drainage system developed in the Nima area since 30 Ma. Given the arid climate conditions, we therefore propose that the fault activity (70-30 Ma) represented by rapid exhumation resulted in a change to topography that triggered the change of water systems. The low relief topography subsequently developed in the arid and tectonically quiescent environments in this area.

Keywords: Low temperature thermochronology; exhumation; internal drainage; low relief topography; Tibet

1 Introduction

Much of the Tibetan Plateau is characterized by low relief topography (LRT) and high elevation (Fielding et al., 1994). In the externally drained regions of the plateau margins, such as the southeast Tibetan Plateau, the low relief surface has been attributed to several mechanisms (Fox et al., 2020), ranging from deep Earth processes such as lower crustal flow (McKenzie and Jackson, 2002; Clack et al., 2006), to drainage area reorganization resulting from horizontal tectonic shortening (Yang et al., 2015) or propagating uplift (Yuan et al., 2021). However, there are relatively few studies on the formation mechanisms of high-elevation, low-relief surfaces in the internally drained regions of the modern Tibetan Plateau interior (Fielding et al., 1994; Liu-Zeng et al., 2008; Hetzel et al., 2011; Han et al., 2019). Liu-Zeng et al. (2008) proposed development of a low-relief surface through establishment of an endorheic river system that promoted bath-tub infilling of the basins from adjacent topography in the central Tibetan Plateau, based on satellite observation of modern plateau landforms. In contrast Hetzel et al. (2011) suggested that peneplanation was driven by an external drainage system removing material to the ocean at low elevation by 50 Ma, that was followed by rapid uplift. Fielding et al. (1994) suggested that the LRT in the Tibetan interior formed in response to the cessation of tectonic activity and onset of climate aridity in the late Cenozoic, and that the slow erosion has managed to remove the pre-existing relief. In a further complexity, the development of low relief has been asynchronous across the Tibetan Plateau (Liu-Zeng et al., 2008; Rohrmann et al., 2012), and has been shown to develop soon after cessation of significant exhumation (e.g. Law and Allen, 2020). Clearly determining the timing of formation of internal drainage, and interaction between the evolution of the drainage system and the low relief topography, are central to understanding the formation and evolution of the plateau landscape.

Low-temperature thermochronology (LTT) methods, such as zircon and apatite (U-Th)/He and apatite fission track, record rock cooling between 200 and 60°C (Reiners et al., 2005). They are commonly used to quantify the long-term exhumation history of mountain belts and determine the climate- and tectonic-driven processes responsible (Reiners and Brandon, 2006). Changes in exhumation may be driven by erosion associated with tectonics or climate. However, as erosion requires potential energy to remove material downhill, higher rates of exhumation require relief, particularly in an internally-drained region where exhumation cannot be effected in high altitude low relief settings by rivers incising to sea level. We use LTT to reconstruct the denudation history of the study area, broadly associating periods of higher exhumation with the presence of topographic relief. We combine our data with sedimentological and palaeoclimate data (DeCelles et al., 2007a, 2007b) to identify the timings and modes of formation of the present landscape.

The Nima and adjacent Lunpola basins are the largest Cenozoic non-marine basins in Central Tibet, whilst the modern day Siling Co, located between the two basins, is the largest saline lake in Tibet (Figure 1b). The Nima Basin has accumulated extensive non-marine deposits from the Late Cretaceous to the Cenozoic, and several studies have investigated the structural geology (Kapp et al., 2007), sedimentary environments (DeCelles et al., 2007a), basin sedimentary provenance (DeCelles et al., 2007a; Kong et al., 2019; Han et al., 2019), paleo-latitude (Meng et al., 2017), and paleo-climate and paleo-elevation (DeCelles et al., 2007b; Wang and Wu, 2015; Deng and Jia et al., 2018) of the region. Here we build on this earlier research with the first LTT study applied to both basin sedimentary rocks and adjacent thrust belt to elucidate the interaction between drainage system, low relief topography and tectonic uplift. We combine zircon U-Pb ages, apatite and zircon (U-Th)/He (AHe and ZHe), and fission track (AFT) thermochronology of granitic and sandstone clasts from the Late Cretaceous to Oligocene Muggar unit in the North Nima Basin, and Xiabie granite in the adjacent Muggar Thrust hanging wall, to elucidate the history of exhumation and long-term evolution of central Tibet landscape.

2 Geological background

The central Tibetan Plateau is mainly comprised of the Lhasa and Qiangtang terranes (Figure 1a). The Bangong−Nujiang and Indus-Yalu sutures in central and southern Tibet, respectively, represent the Late Jurassic to Early Cretaceous Lhasa-Qiangtang and early Cenozoic India-Lhasa collisions (Girardeau et al., 1984; DeCelles et al., 2014; Ding et al., 2016; Zhu et al., 2016; Hu et al., 2016; Li et al., 2019). Marine sedimentation ceased at ~118 Ma (Kapp et al., 2007) in the Bangong-Nujiang suture region because of considerable Cretaceous tectonic shortening (Murphy et al., 1997; Kapp et al., 2003; Volkmer et al., 2007). The N-dipping Shiquanhe-Gaize-Amdo thrust system (SGA) follows the trace of the Bangong-Nujiang suture zone for ~1200 km from Shiquanhe to Amdo (Yin and Harrison, 2000) (Figure 1a). Although the SGA thrust initially slipped in the Early Cretaceous, likely driven by Lhasa-Qiangtang collision, it was re-activated during Cenozoic times during the India-Lhasa collision (e.g. Kapp et al., 2005, 2007; Dewey et al., 1988). An Early Cretaceous granite belt (100-130 Ma), extending from the west in Gaize through northern Nima to northwest Amdo, along the Bangong-Nujiang suture (Figure 1b; Zhu et al., 2016) was most likely related to slab rollback (Yang et al., 2019).

The Nima Basin lies within the Bangong-Nujiang suture zone (Figure 1a). The Early Cretaceous Xiabie granite lies to the north of the Nima Basin (Kapp et al., 2007) in the hanging wall of the Muggar Thrust, which forms the northern boundary to the Basin. The Muggar Thrust is part of the regional system of N-dipping thrust faults of the SGA thrust system (Kapp et al., 2007). The Muggar Thrust separates the Xiabie granite and Triassic-Jurassic deep marine clastics and ophiolitic rocks (Muggar Gangri Complex and Shamuluo Fm.) in the hanging wall, from Late Cretaceous to Cenozoic basinal sedimentary rocks in the footwall. The southern boundary of the Nima Basin is marked by the regionally extensive, southward-dipping Gaize-Siling Co Thrust (Figure 1a).

The Nima Basin comprises Cretaceous-late Miocene sedimentary rocks, which are almost exclusively non-marine, and include volcanic flows, tuffs, alluvial fan deposits, shallow braided stream, eolian dunes and ephemeral lacustrine deposits (DeCelles et al., 2007a). The Lower Muggar unit (Kml; Kapp et al., 2007) is only present in the Northern Nima Basin (Figure 2). It consists of ~400 m of Upper Cretaceous to Paleocene fluvial and eolian sandstones and conglomerates (DeCelles et al., 2007a);

the deposits were dated using palynomorphs. The Upper Muggar unit (Tmu) (Figures 1c and 2; Kapp et al., 2007) is largely composed of lacustrine and fluvial red siltstone, marl, evaporites and conglomerates that were deposited in the late Eocene-Oligocene, dated on the basis of palynomorph data (DeCelles et al., 2007a). Lower and Upper Muggar strata are disrupted by three closely spaced (< 1 km) S-dipping reverse faults, collectively referred to as the Zanggenong Thrusts, likely active at ~40-20 Ma (DeCelles et al., 2007a; Figure 1c).

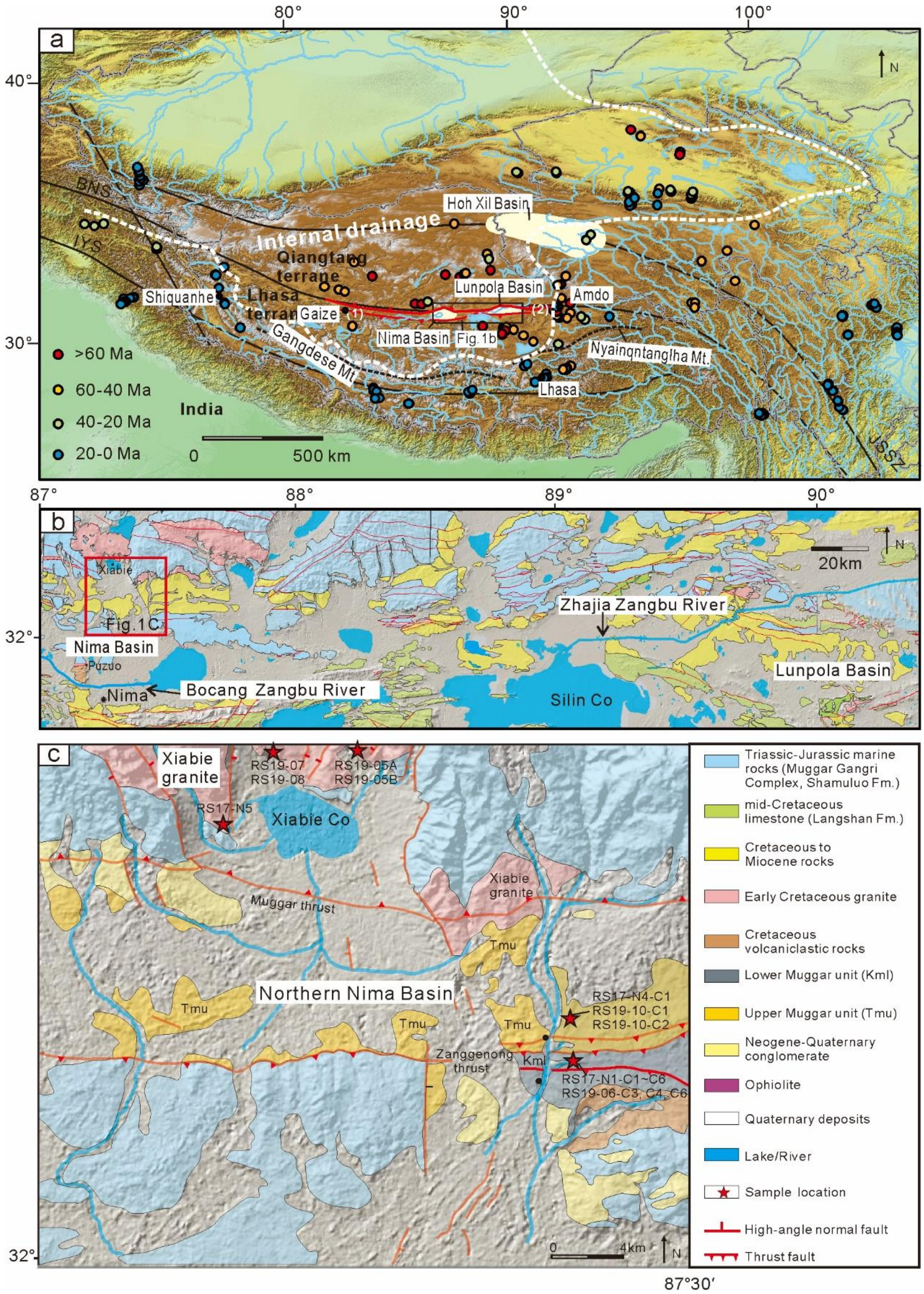

Figure 1. (a) Topographic map of the Tibetan Plateau showing the tectonic framework, modern drainage, and (coloured circles) compilation of timings of cessation of rapid exhumation as determined from published thermal models derived from low

temperature thermochronology data (references provided in Table S1); (1): Gaize-Siling Co Thrust; (2): Shiquanhe-Gaize-Amdo thrust system; IYS: Indus-Yalu suture zone; BNS: Bangong-Nujiang suture zone; JSSZ: Jinshajiang suture zone. (b) Geological map of the Nima-Lunpola area modified from ITGS (2002a, 2002b, 2003a, 2003b, 2006a, 2006b). (c) Geological map of the northern Nima area (DeCelles et al., 2007a) showing sample locations.

3 Sampling and Methods

Eighteen samples were collected from the Nima area as detailed below (Figure 1c; Table 1). Five samples (RS17-N5, RS19-05A, RS19-05B, RS19-08, RS19-07) were collected from the Xiabie granite. One sandstone sample (RS19-09) was collected from the Lower Muggar unit. The twelve conglomerate clasts included 6 granitoid clasts (samples RS19-06-C3, -C4, -C6, RS17-N1-C4, -C5, -C6) and 3 sandstone clasts (RS17-N1-C1, -C2, -C3) from the Lower Muggar unit, and three granitoid clasts (RS19-10-C1, -C2, RS17-N4-C1) from the Upper Muggar unit (Table 1 and Figure 2). Apatite fission track and/or (U-Th)/He analysis were carried out on all samples except sandstone RS19-09, which contained no apatite. The granite (RS17-N5) was used for zircon U-Pb analysis and four granitoid clasts (RS17-N4-C1; RS17-N1-C4, -C5, -C6) were used for zircon (U-Th)/He and U-Pb analysis. In addition, we carried out U-Pb analysis on detrital zircon from the Late Cretaceous sandstone (RS19-09) to complement the existing data from Han et al. (2019).

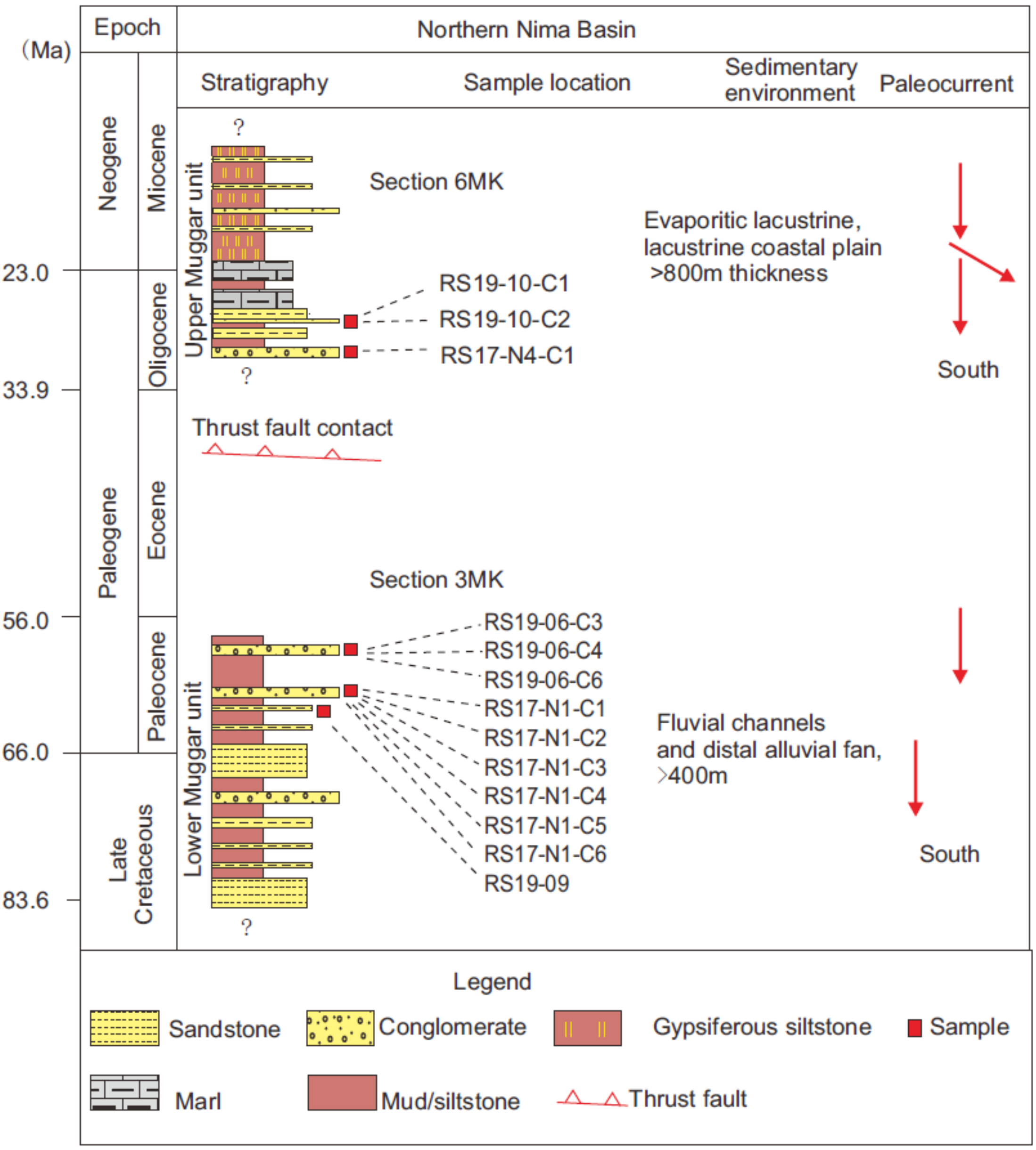

Figure 2. Stratigraphic logs, facies summary and paleocurrent data from the Northern Nima Basin from DeCelles et al. (2007a), showing sample locations for this study. Some samples were collected from the same stratigraphic level, such as granitic clasts (RS17-N1-C6) and sandstone clasts (RS17-N1-C1).

Table 1 Location, analytical methods employed and lithological details of samples from the Northern Nima Basin and Xiabie granite

Number	Sample	Longitude (°E)	Latitude（°N）	Sample position	Lithology	AFT	AHe	Zircon U-Pb	ZHe
1	RS17-N1-C4	87.4168	32.1014	Lower Muggar Unit	granitoid conglomerate clast	√	√	√	√
2	RS17-N1-C5	87.4168	32.1014	Lower Muggar Unit	granitoid conglomerate clast	√	√	√	√
3	RS17-N1-C6	87.4168	32.1014	Lower Muggar Unit	granitoid conglomerate clast	√	√	√	√
4	RS19-06-C3	87.4171	32.1017	Lower Muggar Unit	granitoid conglomerate clast	√	√		
5	RS19-06-C6	87.4171	32.1017	Lower Muggar Unit	granitoid conglomerate clast	√	√		
6	RS19-06-C4	87.4171	32.1017	Lower Muggar Unit	granitoid conglomerate clast	√	√		
7	RS17-N1-C1	87.4168	32.1014	Lower Muggar Unit	buff sandstone conglomerate clast	√	√		
8	RS17-N1-C2	87.4168	32.1014	Lower Muggar Unit	buff sandstone conglomerate clast	√	√		
9	RS17-N1-C3	87.4168	32.1014	Lower Muggar Unit	buff sandstone conglomerate clast	√	√		
10	RS19-09	87.4171	32.1017	Lower Muggar Unit	sandstone			√	
11	RS17-N4-C1	87.4225	32.1139	Upper Muggar Unit	granitoid conglomerate clast	√	√	√	√
12	RS19-10-C1	87.4210	32.1119	Upper Muggar Unit	granitoid conglomerate clast	√	√		
13	RS19-10-C2	87.4210	32.1119	Upper Muggar Unit	granitoid conglomerate clast		√		
14	RS17-N5	87.2241	32.2186	Xiabie granite	granite	√	√	√	
15	RS19-05B	87.2973	32.2615	Xiabie granite	granite	√	√		
16	RS19-08	87.2694	32.2599	Xiabie granite	granite	√			
17	RS19-07	87.2945	32.2607	Xiabie granite	granite	√			
18	RS19-05A	87.3042	32.2447	Xiabie granite	granite	√			

Note: Tick √ represents the analysis technique carried out for every sample

3.1 Zircon U-Pb

Zircon and apatite crystals were extracted by standard crushing and separation techniques. U-Pb dating of zircons was conducted using a LA-ICP-MS at the Laboratory of Earth Surface Process and Environment in Nanjing University (Zhang et al., 2018). Cathodoluminescence (CL) images were used to record the internal structure of zircon grains and select target domains for in-situ U-Pb dating. U-Pb dating of zircons was conducted using an ICP-MS (Agilent 7700x), which was attached to a New Wave 193 nm laser ablation system, following the methods described by Jackson et al. (2004). The laser beam diameter was 25 μm, with a 10-Hz repetition rate and energy of 2–3 J/cm^2. Zircon 91500 was used as the external standard for isotopic fractionation correction, and GJ-1 zircon was used to monitor instrumental reproducibility and stability. The average age of the former (1062 ± 17 Ma, n=60), and latter (603 ± 8 Ma, n=20) overlap the accepted ages (Wiedenbeck et al., 1995; Liu et al., 2010). The software GLITTER (version 4.4) was used to calculate raw data (Griffin, 2008). Common Pb correction was implemented following the method of Andersen (2002). Isoplot 4 software was used for plotting concordance curves and calculating weighted mean age. Zircons with discordance of >10% were excluded in data presentation and interpretation. The complete dataset is reported in Tables S2 and S3.

3.2 Apatite and zircon (U-Th)/He

(U-Th)/He analysis was conducted at the Scottish Universities Environmental Research Centre following procedures of Foeken et al. (2006). In order to avoid the influence of physical properties of apatite and zircon grains such as fragmentation, on age (Brown et al., 2013), we used inclusion-free euhedral crystals with one or two terminations, and a diameter of at least 50 µm. At least five single grains were analyzed for each sample. Grains were packed in Pt tubes and degassed in ultra-high vacuum using an 808 nm diode laser. ^{4}He abundances determined with a Hiden HAL3F quadrupole mass spectrometer (Foeken et al., 2006). Apatite grains were degassed for 60 seconds at 500-600°C and zircon grains were degassed for 20 minutes at 1100-1300°C (Foeken et al., 2006). The degassed apatite packets were spiked with ^{235}U, and ^{230}Th and natural U and Th was measured by ICP-MS (Agilent 7500ce). Where U and Th contents were within 3 times the background value, analytical uncertainties are large and the data are excluded. Degassed zircon grains were extracted from packets prior to dissolution and U-Th analysis were performed following procedures in Dobson et al. (2008). Durango apatite (n=20) and Fish Canyon Tuff zircon (n=15) standards were analysed; the average age of the former is 31.1 ± 1.7 Ma, the latter is 28.3 ± 1.1 Ma, indistinguishable from the ages reported in the literature (Farley et al., 2000; Dobson et al., 2008). AHe and ZHe ages are reported in Tables 2 and 3.

3.3 Apatite fission track determinations

Apatite fission track analysis was performed at the GLOW laboratory, at the University of Glasgow, using either the external detector method (Wildman et al., 2016) or the LA-ICPMS, for U determination (Chew et al., 2016). The U concentration derived from the LA-ICPMS method is consistently lower than that determined from the EDM (Table 4); the discrepancy may be due to internal variation in the concentration of U in apatite grains; given that both methods reproduce the ages of the standards, the AFT ages of the unknown samples are considered accurate in both cases. Apatite grains were mounted in epoxy resin and then polished to reveal a horizontal, internal surface for each crystal; the polished mounts were etched in a 5.5M HNO_3 acid solution, for 20s at 20ºC (Carlson et al., 1999). Tracks were counted using an Axioplan Zeiss microscope (x1250), in both transmitted and reflected light; for each crystal, three Dpar (the diameter of the track etched pits parallel to the c-axis of crystal) measurements were also taken. Either the external detector method (Wildman et al., 2016) or LA-ICPMS were used for U determination. The accuracy of the isotopic determinations derived from the LA-ICP-MS was controlled using the glass standard NIST SRM612 and Durango apatite. The weighted age of Durango apatite is 32.1 ± 1.2 Ma (n=42). The zeta calibration, for the LA-ICPMS method, was performed using Durango fragments (Chew et al., 2016). For the external detector method (EDM), a mica external detector is used; the zeta determination used Durango apatites (31.4 ± 0.5 Ma; Persano, 2003), Mt Dromedary (98.7 ± 0.6 Ma; Persano, 2003), Fish Canyon Tuff (27.9 ± 0.5 Ma; Persano, 2003) and the Shap Granite (75.0 ± 3.1 Ma; Luszczak et al., 2017) standards. Radial plots, created using the free software Isoplot R (Vermeesch, 2018), were used to visualize and analyse the single grain age dispersion (Figure S5).

4 Results and interpretations

4.1 Zircon U-Pb data

We obtained 270 U-Pb zircon dates from six samples. Three granitoid clasts (RS17-N1-C4, RS17-N1-C5, RS17-N1-C6) from the Lower Muggar unit yield weighted mean U-Pb zircon ages of 120.3 ± 0.9 Ma, 119.8 ± 0.9 Ma, and 119.1 ± 1.5 Ma (Figure 3). Granitoid clast RS17-N4-C1 from the Upper Muggar unit yields a U-Pb zircon age of 119.8 ± 1.0 Ma. Xiabie granite sample RS17-N5 from the Muggar Thrust hanging wall yields a weighted mean zircon U-Pb age of 119.7 ± 1.1 Ma. The 137 zircon U-Pb ages from a sandstone sample (RS19-09) from the Lower Muggar unit exhibit a distinct cluster at 100-130 Ma, with ages extending to >2500 Ma (Figure 3). The weighted mean age (67.0 ± 2.0 Ma) of the three youngest grains of sample RS19-09 constrains the maximum depositional ages of the Lower Muggar unit (Dickinson and Gehrels, 2009).

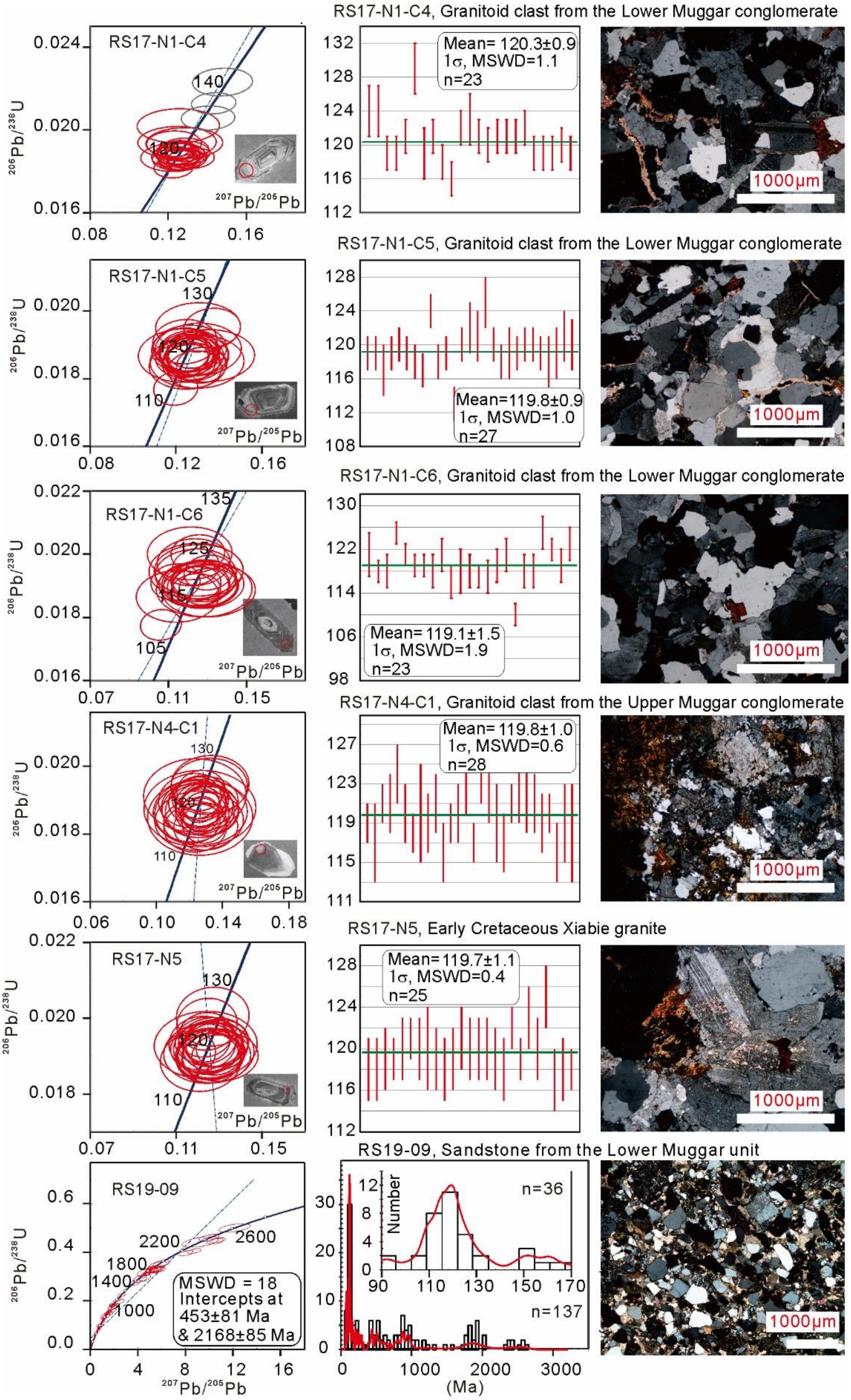

Figure 3. Zircon U-Pb dating results and thin section photos for granitoid clasts (RS17-N1-C4, N1-C5, N1-C6, N4-C1), and the sandstone (RS19-09) and granite sample (RS17-N5) from the Northern Nima Basin and Xiabie granite.

4.2 Apatite/zircon U-Th/He data

As the recoil correction (Ft) factor may over or under-correct AHe or ZHe depending on rates of diffusion and parent element distribution (e.g., Wildman et al., 2016), uncorrected AHe and ZHe ages are reported below, and the effect of alpha ejection incorporated during the thermal history inversion modeling. Although some samples yield dispersed single crystal ages, there is no analytical reason to discard them. For a more comprehensive report of all (U-Th)/He ages including the ‘outliers’, Table 2 and 3 presents all the single-grain (U-Th)/He ages; the mean is calculated using only those ages that are within 20% of the standard deviation (Flowers and Kelley, 2011).

Single-grain apatite (U-Th)/He analyses were performed on fourteen samples (Table 2). Five apatite grains from RS19-05B (Xiabie granite) yield AHe ages ranging from 30 to 50 Ma. Sample RS17-N5 from the Xiabie granite has a mean AHe age of 41 ± 6 (1σ) Ma. Apatite grains from two granitoid clasts (RS17-N4-C1, RS19-10-C1) from the Upper Muggar unit yield mean AHe ages of 36 ± 4 Ma and 28 ± 5 Ma, respectively. Sample RS19-10-C2 from the Upper Muggar unit yields individual AHe ages ranging from 13 to 43 Ma. Four samples RS17-N1-C4, RS17-N1-C5, RS19-06-C3, RS19-06-C6 from the Lower Muggar unit yield mean AHe ages of 38 ± 3 Ma, 31 ± 6 Ma, 31 ± 6 Ma, 25 ± 3 Ma, respectively. Two samples (RS17-N1-C6 and RS19-06-C4) from the Lower Muggar unit yield individual AHe ages ranging from 20 to 47 Ma, and 35 to 62 Ma, respectively. Fifteen apatite grains from three sandstone clasts (RS17-N1-C1, -C2, -C3) from the Lower Muggar unit yield individual AHe ages ranging from 9 to 21 Ma, 12 to 29 Ma and 8 to 19 Ma, respectively.

Seven of the fourteen samples yield single-grain AHe ages with > 20% standard deviation of the mean. Four of fourteen samples show a weak positive correlation between uncorrected AHe ages and eU (RS17-N1-C1, RS17-N1-C5, RS19-06-C6, RS17-N4-C1). Two samples (RS17-N1-C2, RS19-10-C2) show a weak negative correlation between age and eU. Similarly, except for RS17-N1-C2, RS17-N1-C3, RS17-N1-C6 and RS17-N4-C1 (Figures S2 and S3), there is no evident correlation between AHe age and grain size. The absence of clear correlations suggests that the age dispersion reflects some combination of eU variation (Gautheron., 2009; Flower et al., 2009; Guenthner et al., 2013), differences in grain radii (Reiners et al., 2001), grain fragmentation (Brown et al., 2013), undiscovered inclusions (Vermeesch et al., 2007), and/or implantation of ^{4}He (Farely et al., 1996). The (U-Th)/He age of apatites from sandstone clasts of the Lower Muggar unit are generally younger than those of granitoid conglomerate clasts. This may be caused by the fact that most of the detrital apatites in the sandstone clasts are broken and with a heavily pitted surface that may suggest U precipitation from circulating fluids (Brown et al., 2013).

A few Ft-corrected AHe ages from the granitoid clasts from the Lower Muggar unit are slightly older than same-sample AFT ages. This has been previously recorded in samples that experienced a period of burial followed by erosional unroofing (Flowers et al., 2009; Ault et al., 2009). Radiation damage increases the closure temperature of ^{4}He in apatite (e.g., Flowers et al., 2009; Gautheron et al., 2009) and its effect on samples characterized by reheating in the PRZ and PAZ are known to be amplified.

Whereas the dispersion of AHe ages from rocks that experienced no or very little burial (e.g., the Xiabie granite and the Upper Muggar unit) can be accounted for in the thermal modelling (Figure S1), in the case of the Lower Muggar sedimentary rocks that were buried at temperatures high enough to almost completely reset the AFT ages, some of the AHe ages are not reproduced by the inversion models (Figure S1). These observations suggest that a major driver of the over-dispersion is our inability to capture the diffusion process when radiation damage and partial annealing occur contemporaneously, at different rates, depending on their original track lengths and apatite chemical composition (Flowers et al., 2009; Gautheron et al., 2009).

Eleven zircon grains from two granitoid clasts (RS17-N1-C4 and -C6) from the Lower Muggar unit yield individual He ages ranging from 58 to 107 Ma and 74 to 105 Ma (Table 3). Seven zircon grains from sample RS17-N1-C5 from the Lower Muggar unit yield a mean ZHe ages of 84 ± 9 Ma. Another seven zircon grains from sample RS17-N4-C1 from the Upper Muggar unit yield a mean age of 67 ± 6 Ma. A negative uncorrected ZHe ages-eU correlation is observed for three samples (RS17-N1-C4, -C5, -C6) from the Lower Muggar unit (Figure S4), suggesting that radiation damage facilitates He diffusion and, at least partially, drives age dispersion (Guenthner et al., 2013; 2014). Sample RS17-N1-C4 displays a positive ZHe age-eU correlation for concentrations of U up to 800-1000 ppm; for higher concentrations, the correlation is negative (Figure S4). This suggests that, at low U concentrations, radiation damage is not sufficient to affect He diffusion and the U concentration increases radiation damage to form a network of linked voids that promotes diffusion

(Guenthner et al., 2013). A few Ft corrected ZHe ages are slightly older than the time of intrusion, probably an effect of still poorly understood interaction between alpha ejection (Farley et al., 1996, 2002), radiation damage effects (Guenthner et al., 2013), U-Th-zonation (Dobson et al., 2008; Danisik et al., 2017) and He diffusion (Reiners et al., 2006; Guenthner et al., 2013).

Table 2. Results of Apatite (U-Th)/He Analysis

Grain name	^{4}He (cc)	^{238}U (ng)	^{232}Th (ng)	eU ppm	[a]T	[b]L (um)	[c]W (um)	Ft	Th/U	Raw age (Ma)	error (Ma)	Cor. Age (Ma)	error (Ma)	Ave. Raw age and SD (Ma)	Ave. Cor. Age And SD (Ma)
RS17-N1-C1-02	2.3E-10	0.019	0.308	28.5	0	120	103	0.7	15.8	20.7	0.8	28.6	1.2		
RS17-N1-C1-03	2.1E-10	0.021	0.229	33.6	0	110	90	0.7	10.7	23.4	0.3	34.1	0.5		
RS17-N1-C1-05	2.8E-10	0.051	0.202	48.2	0	100	90	0.7	4.0	23.7	0.3	34.9	0.4		
RS17-N1-C1-06	2.3E-10	0.037	0.293	26.7	0	130	110	0.7	8.0	17.8	0.2	24.0	0.3		
RS17-N1-C1-07	8.0E-11	0.019	0.244	41.8	0	100	85	0.7	13.1	8.7	0.1	13.0	0.2	/	/
RS17-N1-C2-02	6.0E-11	0.008	0.040	14.3	0	90	73	0.6	5.2	29.1	1.4	47.6	2.2		
RS17-N1-C2-03	8.7E-11	0.015	0.050	16.4	0	100	80	0.7	3.4	27.2	1.0	41.9	1.5		
RS17-N1-C2-04	9.2E-11	0.012	0.087	26.0	0	100	70	0.6	7.4	23.4	0.6	38.1	0.9		
RS17-N1-C2-05	5.2E-11	0.003	0.075	25.4	0	90	60	0.6	23.5	20.8	0.6	37.4	1.1		
RS17-N1-C2-06	9.9E-11	0.035	0.140	94.4	0	80	60	0.5	3.9	11.9	0.4	22.0	0.8	/	/
RS17-N1-C3-01	7.4E-11	0.017	0.131	37.7	0	90	75	0.6	7.6	12.6	0.2	20.3	0.4		
RS17-N1-C3-02	2.7E-11	0.012	0.026	19.4	0	90	65	0.6	2.1	12.0	0.7	20.7	1.2		
RS17-N1-C3-03	4.6E-11	0.018	0.126	23.2	0	100	90	0.7	7.1	8.0	0.1	11.8	0.2		
RS17-N1-C3-04	7.1E-11	0.018	0.081	20.3	0	100	85	0.7	4.5	15.7	0.4	23.7	0.6		
RS17-N1-C3-05	1.7E-10	0.028	0.181	28.2	0	110	95	0.7	6.5	19.4	0.3	27.7	0.4	/	/
RS17-N1-C4-1	1.8E-10	0.012	0.121	48.1	1	110	55	0.5	10.1	35.9	0.5	65.8	0.9		
RS17-N1-C4-2	3.1E-10	0.032	0.170	44.2	1	140	68	0.6	5.3	35.4	0.5	55.8	0.8		
RS17-N1-C4-3	6.6E-10	0.021	0.455	101.0	1	140	60	0.6	21.7	42.2	0.6	70.8	1.0	37.8 ± 3.1	64.2 ± 6.2
RS17-N1-C5-1A	3.7E-10	0.042	0.272	34.4	1	160	88	0.7	6.5	28.7	0.3	40.5	0.5		
RS17-N1-C5-2A	1.5E-10	0.024	0.127	44.7	1	160	55	0.6	5.2	23.1	0.4	40.3	0.7		
RS17-NI-C5-1	3.8E-10	0.046	0.236	24.9	2	200	90	0.7	5.1	30.4	0.4	41.7	0.5		

RS17-NI-C5-3	7.5E-10	0.096	0.354	31.1	1	200	107	0.8	3.7	34.2	0.4	45.1	0.5		
RS17-NI-C5-4	8.5E-10	0.068	0.429	76.0	1	180	70	0.7	6.3	41.5	0.5	63.0	0.7		
RS17-NI-C5-5	6.1E-10	0.106	0.313	14.5	1	300	128	0.8	3.0	28.1	0.3	35.1	0.4	31.0 ± 5.7	44.3 ± 8.8
RS17-N1-C6-2	5.6E-10	0.043	0.375	54.8	2	170	75	0.7	8.6	35.1	0.5	52.0	0.7		
RS17-N1-C6-3	6.3E-10	0.043	0.307	60.3	2	155	70	0.6	7.2	45.1	0.6	69.4	0.9		
RS17-N1-C6-4	3.2E-10	0.066	0.279	59.9	2	155	75	0.7	4.3	20.1	0.2	30.0	0.3		
RS17-N1-C6-2a	1.1E-09	0.108	0.488	157.3	1	137	64	0.6	4.5	41.8	1.0	67.9	1.6		
RS17-N1-C6-3a	3.3E-10	0.033	0.237	49.1	1	140	72	0.6	7.1	30.8	1.5	47.5	2.3		
RS17-N1-C6-4a	3.8E-10	0.028	0.163	44.7	2	140	65	0.6	5.8	46.5	0.7	74.9	1.1		
RS17-N1-C6-6a	5.2E-10	0.098	0.423	72.6	1	150	85	0.7	4.3	21.5	0.2	30.8	0.3	/	/
RS19-06-C3-3	2.8E-10	0.011	0.264	39.0	2	160	68	0.60	23.64	31.62	0.5	52.8	0.8		
RS19-06-C3-5	2.9E-10	0.019	0.242	32.5	2	157	77	0.63	12.78	30.96	0.5	48.8	0.7		
RS19-06-C3-1c	9.6E-11	0.011	0.121	18.3	2	130	81	0.63	10.90	19.94	0.5	31.7	0.8		
RS19-06-C3-2c	1.1E-10	0.014	0.051	11.3	2	157	77	0.65	3.58	35.98	1.6	55.6	2.5		
RS19-06-C3-3c	1.7E-10	0.022	0.075	10.3	2	190	89	0.70	3.46	36.10	1.1	51.7	1.6	30.9 ± 5.9	48.1 ± 8.5
RS19-06-C4-1	6.1E-10	0.058	0.359	21.2	2	210	113	0.74	6.14	34.89	0.3	46.4	0.4		
RS19-06-C4-2	4.8E-10	0.024	0.196	22.4	2	180	83	0.67	8.11	55.50	0.6	82.2	0.8		
RS19-06-C4-3	7.9E-10	0.054	0.209	11.7	2	236	122	0.77	3.87	62.40	0.6	80.5	0.8		
RS19-06-C4-4	9.2E-10	0.099	0.454	42.4	1	232	91	0.73	4.58	36.60	0.3	49.6	0.4	/	/
RS19-06-C6-1	8.4E-11	0.013	0.122	20.2	2	130	80	0.63	9.18	16.10	0.2	26.0	0.3		
RS19-06-C6-2	1.1E-10	0.014	0.076	12.8	2	152	80	0.65	5.54	28.44	0.3	44.5	0.5		
RS19-06-C6-3	2.5E-10	0.026	0.207	29.3	0	163	79	0.65	7.82	27.33	0.3	41.8	0.4		
RS19-06-C6-4	1.3E-10	0.015	0.147	24.4	1	159	72	0.65	9.61	21.28	0.2	32.8	0.4		
RS19-06-C6-5	2.0E-10	0.014	0.166	26.6	1	130	78	0.67	11.49	29.93	0.3	44.3	0.5		
RS19-06-C6-1C	4.4E-10	0.050	0.406	26.7	2	183	109	0.72	8.17	24.78	0.2	34.2	0.3	24.6 ± 4.7	37.3 ± 6.8
RS19-10-C1-1	3.3E-10	0.021	0.341	60.3	2	130	72	0.60	15.96	26.69	0.3	44.9	0.6		

RS19-10-C1-2	2.8E-10	0.011	0.296	56.8	2	123	68	0.57	27.77	28.13	0.4	49.3	0.7		
RS19-10-C1-3	1.8E-10	0.020	0.101	22.8	2	160	69	0.62	4.98	32.71	0.8	52.8	1.3		
RS19-10-C1-4	3.5E-10	0.029	0.258	40.2	2	150	77	0.63	9.03	32.45	0.4	51.4	0.7		
RS19-10-C1-5	1.1E-10	0.016	0.122	26.3	1	118	76	0.66	7.49	19.53	0.4	29.6	0.7	27.9 ± 4.8	45.6 ± 8.4
RS19-10-C2-1	2.0E-10	0.037	0.355	71.1	2	147	68	0.60	9.62	13.38	0.2	22.4	0.3		
RS19-10-C2-2	4.5E-10	0.029	0.389	37.2	2	184	84	0.67	13.34	30.37	0.4	45.7	0.5		
RS19-10-C2-3	4.4E-10	0.038	0.222	29.7	1	183	81	0.69	5.87	40.36	0.6	58.2	0.8		
RS19-10-C2-4	2.6E-10	0.021	0.127	18.9	2	162	81	0.66	6.12	42.93	0.9	65.3	1.4		
RS19-10-C2-5	2.4E-10	0.020	0.175	26.6	1	141	80	0.68	8.96	32.22	0.6	47.4	0.8	/	/
RS17-N4-C1-1A	3.0E-10	0.031	0.142	26.8	1	170	75	0.7	4.6	38.3	0.6	56.8	0.9		
RS17-N4-C1-1	2.8E-10	0.033	0.154	16.4	2	200	92	0.7	4.6	33.2	0.4	45.3	0.5		
RS17-N4-C1-2	8.3E-10	0.074	0.380	65.4	1	250	63	0.6	5.2	41.9	0.4	74.8	0.8		
RS17-N4-C1-3	8.4E-10	0.070	0.613	55.1	1	200	88	0.7	8.7	32.1	0.4	44.1	0.5		
RS17-N4-C1-4	9.7E-10	0.128	0.510	42.9	1	180	113	0.8	4.0	31.9	0.4	41.4	0.5	35.7 ± 7.4	51.6 ± 3.5
RS19-05B-1	4.2E-10	0.054	0.219	45.3	2	146	80	0.65	4.06	32.97	0.5	50.9	0.7		
RS19-05B-2A	1.7E-10	0.021	0.075	18.6	2	170	70	0.63	3.53	36.20	1.1	57.5	1.8		
RS19-05B-3	5.0E-10	0.073	0.265	73.4	1	149	70	0.62	3.64	30.10	0.4	48.5	0.6		
RS19-05B-4	3.1E-10	0.046	0.165	58.3	2	110	72	0.60	3.60	29.58	0.5	49.6	0.8		
RS19-05B-5	3.6E-10	0.036	0.099	26.3	1	180	71	0.64	2.75	49.80	1.2	77.8	1.8	/	/
RS17-N5-1	1.8E-10	0.021	0.087	22.4	2	175	65	0.6	4.1	35.0	0.5	55.1	0.7		
RS17-N5-2	3.0E-10	0.028	0.098	40.7	1	140	60	0.6	3.5	47.1	0.7	79.2	1.1	41.1 ± 6.1	67.1 ± 12.0

Note. a. T——termination; b. L——length; c. W——width; For samples with standard deviation greater than 20%, the mean age is not calculated (Flowers and Kelley, 2011).

347 Table 3. Results of Zircon (U-Th)/He Analysis

Grain name	^{4}He (cc)	^{238}U (ppm)	^{232}Th (ppm)	eU (ppm)	^{c}T	^{a}L (um)	^{b}W (um)	F(T)	Th/U	Raw age (Ma)	Error (Ma)	Corrected age (Ma)	Error (Ma)	Ave. Raw age and SD (Ma)	Ave. Cor. Age and SD (Ma)
RS17-N1-C4-Z1	2.49E-08	588.88	361.23	673.77	2	200	75	0.74	0.61	106.70	5.95	113.11	8.01		
RS17-N1-C4-Z2	6.92E-09	373.14	424.29	472.85	2	180	65	0.71	1.14	62.66	4.45	88.73	6.31		
RS17-N1-C4-Z3	1.64E-08	1107.38	516.58	1228.78	2	190	53	0.67	0.47	82.73	4.61	97.41	6.90		
RS17-N1-C4-Z4	2.31E-09	217.60	318.86	292.54	2	150	55	0.65	1.47	56.55	4.06	86.41	6.22		
RS17-N1-C4-Z5	1.04E-08	925.97	533.22	1051.27	2	170	50	0.64	0.58	75.55	5.35	117.72	8.35		
RS17-N1-C4-Z6	1.05E-08	980.32	461.13	1088.68	2	130	53	0.64	0.47	87.39	4.88	107.25	7.61		
RS17-N1-C4-Z7	9.86E-09	1249.02	651.77	1402.18	2	130	55	0.65	0.52	58.21	4.12	89.13	6.31	/	/
RS17-N1-C5-Z1	8.15E-09	870.23	767.37	1050.57	2	140	50	0.63	0.88	72.04	5.11	114.90	8.15		
RS17-N1-C5-Z2	2.68E-08	1866.43	1223.56	2153.97	2	150	60	0.68	0.66	74.85	5.29	109.98	7.77		
RS17-N1-C5-Z3	2.38E-08	1596.10	723.78	1766.19	2	190	55	0.67	0.45	76.21	5.38	113.89	8.04		
RS17-N1-C5-Z4	1.04E-08	560.04	398.59	653.71	2	180	55	0.67	0.71	94.72	6.71	142.33	10.08		
RS17-N1-C5-Z5	1.61E-08	847.21	542.20	974.63	2	180	65	0.71	0.64	70.79	5.01	100.01	7.07		
RS17-N1-C5-Z6	2.17E-08	1346.13	755.57	1523.68	2	160	60	0.68	0.56	80.52	5.69	118.61	8.38		
RS17-N1-C5-Z7	8.08E-09	418.03	516.81	539.48	2	150	53	0.64	1.24	117.41	8.36	182.36	12.98	78 ± 9	117 ± 14
RS17-N1-C6-Z1	1.57E-08	1168.61	414.97	1266.13	2	170	53	0.66	0.36	86.17	6.09	131.54	9.29		
RS17-N1-C6-Z2	1.24E-08	1105.77	732.77	1277.97	2	170	50	0.64	0.66	74.17	5.25	115.93	8.20		
RS17-N1-C6-Z3	1.60E-08	1532.07	830.99	1727.35	2	150	50	0.64	0.54	80.08	5.66	125.99	8.90		
RS17-N1-C6-Z4	5.24E-09	440.67	409.93	537.00	2	120	50	0.62	0.93	105.48	7.54	169.78	12.13	86 ± 14	136 ± 24
RS17-N4-C1-Z1	3.83E-09	198.38	185.40	241.95	2	210	59	0.69	0.93	70.34	5.02	102.02	7.28		
RS17-N4-C1-Z2	6.94E-09	198.17	215.01	248.70	2	220	78	0.75	1.08	68.65	4.88	92.01	6.54		
RS17-N4-C1-Z3	1.30E-08	354.01	331.52	431.91	2	280	70	0.73	0.94	71.16	5.04	97.09	6.88		
RS17-N4-C1-Z4	1.16E-08	228.66	211.63	278.39	2	250	95	0.79	0.93	59.94	4.25	75.62	5.36		

RS17-N4-C1-Z5	7.10E-09	293.59	245.53	351.29	2	200	75	0.74	0.84	58.47	4.15	78.81	5.59		
RS17-N4-C1-Z6	1.99E-08	474.62	469.85	585.04	2	260	75	0.75	0.99	75.77	5.37	101.11	7.16		
RS17-N4-C1-Z7	4.35E-09	152.32	162.25	190.45	2	240	70	0.73	1.07	63.24	4.50	86.26	6.14	67 ± 6	90 ± 11

Note. a. L——length; b. W——width; c. T——termination. For samples with standard deviation greater than 20%, the mean age is not calculated (Flowers and Kelley, 2011).

4.3 Apatite fission track data

Sixteen samples were dated using single-grain apatite fission track (AFT) analysis (Table 4). Five Xiabie granite samples (RS19-05A, -05B, -07, -08, and RS17-N5) were analysed; four yielded AFT ages between 43 ± 5 Ma and 57 ± 4 Ma, with one significantly older (89 ± 10 Ma; Table 4). Two granitoid clasts from the Upper Muggar Unit yielded AFT ages of 51 ± 5 Ma and 67 ± 5 Ma. Four of the six granitoid clasts (RS17-N1-C6, RS19-06-C3, -C4, -C6) from the conglomerate beds (Lower Muggar unit) yielded AFT ages ranging from 31 ± 3 Ma to 34 ± 3 Ma, younger than their stratigraphic age. Two other granite clasts (RS17-N1-C4, -N1-C5) from the Lower Muggar unit yielded older apatite fission track ages, 62 ± 10 Ma to 77 ± 15 Ma, which overlap the conglomerate depositional age. The AFT ages of 3 sandstone clasts (RS17-N1-C1, -C2, -C3) from the Lower Muggar unit range from 50 ± 7 Ma to 83 ± 10 Ma. In summary, all the AFT central ages are either younger than or overlap the depositional age of the Lower Muggar unit.

The low U concentration of many apatite crystals and their small size hampered identification of horizontal confined tracks (Donelick et al., 2005). Consequently, few tracks were measured, and no samples had a statistically significant track length distribution; they were nonetheless used in thermal modelling. Four of the granitoid samples (RS19-05B; RS17-N5, RS17-N1-C4, RS17-N1-C5) failed the chi-square test ($P(\chi 2) <0.05$), and three of them (RS17-N1-C5, RS17-N1-C4, RS17-N5) have high dispersion (>37%). These three samples were measured by the LA-ICP-MS method. Ketcham et al. (2018) noted that LA-ICP-MS derived AFT ages are commonly characterized by a dispersion of the single grain ages that is larger than those obtained by the EDM method. We suggest that this is due to the local variability of U concentration sampled by LA-ICP-MS spot analysis that may not be representative of the bulk apatite value (Cogne et al., 2021). This is supported by the observation that the three samples (RS17-N1-C5, RS17-N1-C4, RS17-N5) with the lowest U concentration (2.1-4.8 ppm; Table 4) have the oldest AFT ages (cf. McDannell et al., 2019; Fernie et al., 2018). Irrespective of the method used to calculate the AFT ages, high dispersion is likely related to prolonged residence within the PAZ, rather than to the preservation of the original detrital age population, as the AFT ages are similar or younger than the stratigraphic age.

Table 4. Results of Apatite Fission Track Analysis

Sample	No. of Grains .	$^a\rho_s$ ($10^5/cm^2$)	Total ^bN_S	$^a\rho_i$ ($10^5/cm^2$)	Total ^bN_i	$^a\rho_d$ ($10^5/cm^2$)	^bN_d	$^cP(\chi)^2$	$^dD_{par}$ (μm)	^{238}U ppm	Central AFT Age (Ma)	±1σ	Pooled AFT Age (Ma)	±1σ	Dis. (%)	MTL c Axis Correction (μm)	SD (μm)	N^e
RS19-05-A	16	5.1	250	32.0	1562	17.7	14503	0.50	1.5	25.3	42.5	5.3	42.5	2.9	0	13.5	1.4	8
RS19-05-B	20	7.4	368	31.1	1556	16.1	14503	0.02	1.5	28.4	57.1	4.4	57.1	3.3	20	13.96	1.2	27
RS19-08	17	3.1	263	17.8	1488	18.8	14503	0.60	1.6	14.9	50.0	3.3	49.0	3.3	0	14.33	1.1	9
RS19-07	12	5.4	209	25.5	990	18.1	14503	0.17	1.6	23.6	56.9	7.7	57.2	4.4	11	13.41	1.3	15
RS17-N5*	22	5.2	179	-	-	-	-	0.00	1.1	2.1	89.0	10	96.8	7.3	37	12.48	1.3	5
RS19-10-C1	20	5.7	196	23.5	810	18.4	14503	0.43	1.5	17.4	67.0	5.3	67.0	5.3	0	13.44	1.2	4
RS17-N4-C1*	14	4.8	174	-	-	-	-	0.09	1.4	3.8	51.3	4.8	51.3	3.9	19	12.29	0.5	2
RS19-06-C3	12	2.1	93	15.8	697	16.5	14503	0.23	1.6	15.8	33.0	4.1	33.1	3.7	18	-	-	0
RS19-06-C4	20	2.0	189	14.2	1317	14.5	14503	0.10	1.5	13.5	31.2	2.9	31.3	2.4	19	13.24	0.6	3
RS19-06-C6	20	2.0	170	15.6	1313	17.3	14503	0.10	1.6	12.9	33.4	3.4	33.6	2.7	24	14.45	1.0	3
RS17-N1-C6*	20	2.0	124	-	-	-	-	0.69	1.3	2.2	33.6	3.0	33.6	3.0	0	-	-	0
RS17-N1-C4*	18	3.4	129	-	-	-	-	0.00	1.2	2.3	62.0	10.0	71.0	6.3	56	12.70	0.2	3
RS17-N1-C5*	9	4.5	57	-	-	-	-	0.03	1.2	4.8	77.0	15.0	77.0	10	39	-	-	0
RS17-N1-C1	26	5.4	313	19.8	1143	12.5	8790	0.04	1.7	23.5	53.1	4.3	51.7	10.8	22	13.30	0.6	6
RS17-N1-C2	11	4.6	69	17.5	262	12.4	8790	0.89	1.8	20.6	49.7	6.7	49.3	10.3	0	12.26	1.0	5
RS17-N1-C3	20	13.6	481	30.8	1091	12.2	8790	0.00	2.0	36.1	83.0	10.0	81.0	16.9	47	12.78	1.5	15

*Concentration of U measured by LA-ICP-MS

a. $\rho_{(i,s,d)}$ are track density of induced, spontaneous, dosimeter tracks.

b. Ni, Ns, and Nd are the number of induced, spontaneous, and dosimeter tracks counted.

c. $P(\chi)2$ value of the chi-square age homogeneity test.

d. Dpar measurements are etch pit diameters used as a proxy for the influence of chemical composition on track annealing [Donelick et al., 2005]. Three to five Dpar measurements were used for each grain.

e. The number of confined tracks

5 **Thermal histories**

5.1 Thermal Modelling method

Although the number of measured track lengths was often low, the combination of the apatite fission ages and single-grain ZHe and AHe ages made it possible to invert thermal histories. Single-sample AFT and AHe/ZHe ages were combined in the software QTQt (5.4.2) and used to derive thermal histories that best fit the thermochronological data (Gallagher, 2012). We used the radiation damage models of Flowers et al. (2009), Gautheron et al. (2009) and Guenthner et al. (2013) to describe ^{4}He diffusion of apatite and zircon. For the apatite fission track data, the multi-kinetic annealing model of Ketcham et al. (2007) was applied, using Dpar values as the kinetic parameter. Few tracks were measured, thus the models were run without track length data. Uncorrected ZHe and AHe ages were used. Constraint boxes of 10 ± 10°C (assumed surface temperature) at 70 ± 10 Ma, and 10 ± 10°C at 30 ± 10 Ma were used for modelling of the Lower Muggar unit and Upper Muggar unit respectively, based on their stratigraphic age. Using the analytical uncertainty on individual ages likely underrepresents the true uncertainty (Flowers et al., 2015), so a 10% uncertainty was given by QTQt software for each single grain (AHe and ZHe) age when running the thermal model (Gallagher, 2012).

The thermal modelling strategy and model parameters are reported in the supporting information (Text S1, Table S4). The data were scrutinized following the recommendations of Flowers and Kelley (2011); of the thirteen samples that yielded both AFT and AHe ages, only 10 were modelled. One of these (RS17-N4-C1) includes ZHe data. Three samples were discarded due to the overdispersion of either the single grain AFT ages (granitic clast sample RS17-N1-C4 and granite RS17-N5), or the AHe determinations (granitoid clast RS19-06-C4).

5.2 Thermal modelling results

Sample RS19-05B from the Xiabie granite produced a thermal history characterized by cooling between 70-40 Ma, from 100 to 20°C at a rate of ~3°C/Ma, followed by a transition to slow cooling (0.25°C/Myr), with one order of magnitude difference between the two values. The two granite clasts (RS17-N4-C1 and RS19-10-C1) from the Oligocene Upper Muggar unit show a similar history, recording cooling at 70-40 Ma, with sample RS17-N4-C1 residing for a long time in the apatite partial annealing zone prior to cooling (Figure 4).

The seven conglomerate clasts from the Late Cretaceous Lower Muggar unit show similar thermal histories (Figure 4). These seven clasts are characterized by moderate heating at ~70-40 Ma, but exhumation occurs at different rates. Four granite clasts (RS17-N1-C5, -C6, and RS19-06-C3, -C6) show rapid cooling through the apatite partial retention zone (80-40°C）, beginning at 40 Ma and reaching near-surface temperatures by 30 Ma. The two sandstone clasts RS17-N1-C1 and RS17-N1-C2 show pulses of rapid cooling at 40-30 Ma and 50-30 Ma respectively, from 100 to 30°C (Figure 4). RS17-N1-C3 records monotonic cooling starting at ~40 Ma. Except for sample RS17-N1-C3, the rapid cooling rate of the other six samples from the

Lower Muggar unit ranges from ~6°C to ~8°C/Myr, decreasing to approximately 0.25°C ~1°C/Myr after ~30 Ma.

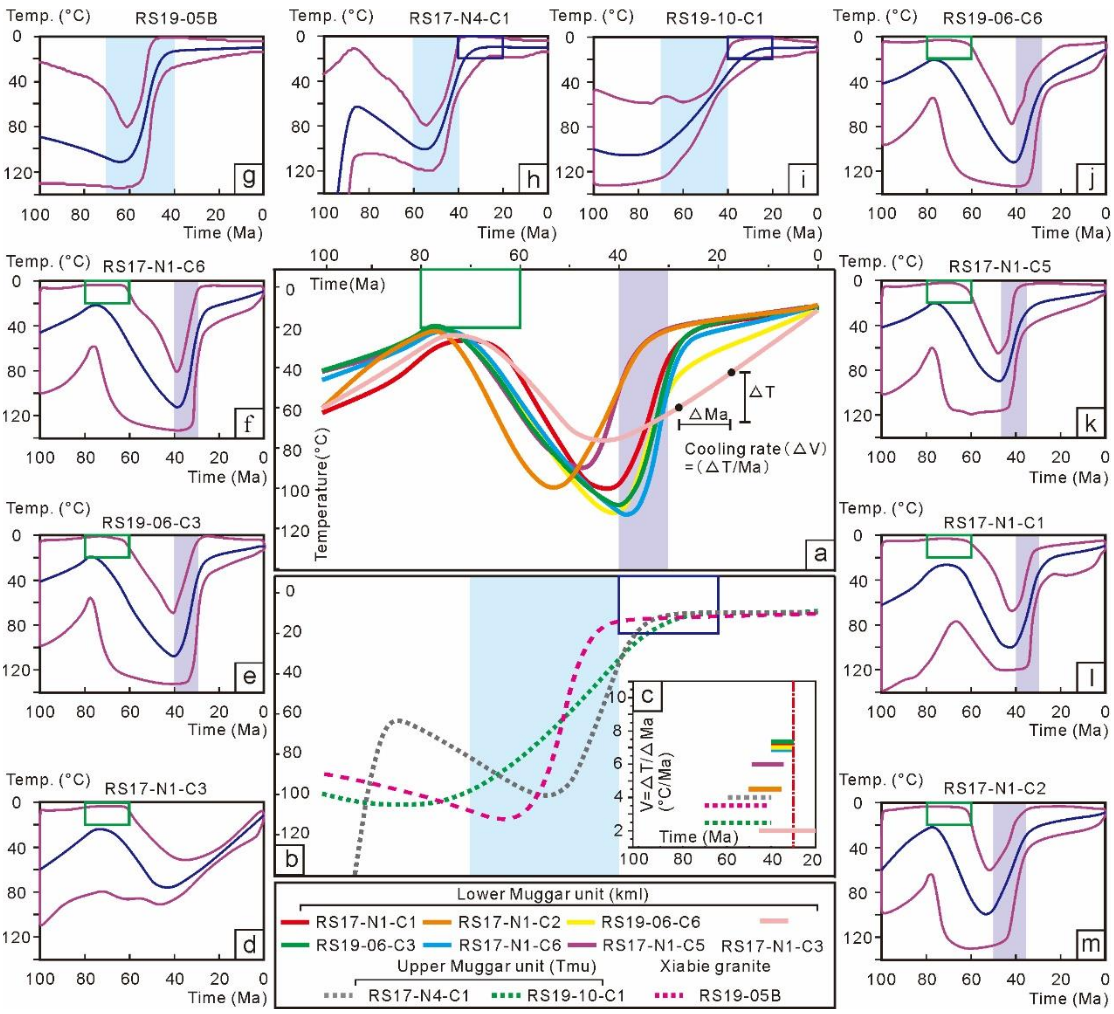

Figure 4. Thermal history models for Late Cretaceous to Oligocene conglomerate clasts of the North Nima Basin and for the Xiabie granite. (a) The expected model for 4 granitoid and 3 sandstone clasts from the Lower Muggar unit, highlighting 40-30 Ma cooling episode. The green box represents the sample at surface temperature from 80-60 Ma. (b) Expected model for one granite sample from the Xiabie granite and 2 granitoid clasts from the Upper Muggar unit, highlighting 70-40 Ma cooling. The blue box represents sample at surface temperature from 40-20 Ma. (c) Cooling rate of each

sample over specified time period. (d-m) Expected thermal history model with 95% confidence interval for each sample.

6 Discussion

6.1 Age and provenance of the Late Cretaceous-Cenozoic sediments in the Nima-Lunpola Basin

The weighted mean age of the three youngest detrital zircon grains from the Lower Muggar unit (67 ± 2 Ma; section 4.1) is consistent with palynomorph results (DeCelles et al., 2007a), indicating it was deposited during the Late Cretaceous (Senonian) to Early Paleocene. Likewise, the weighted mean of the two youngest U-Pb zircon ages of the Upper Muggar unit (35 ± 2 Ma; Han et al., 2019) is consistent with palynomorph results indicating it was deposited in the late Eocene-Oligocene (DeCelles et al., 2007a).

In the Nima-Lunpola basin, the provenance of zircons from all sandstone samples (i.e. the Late Cretaceous-Paleocene Lower Muggar sandstone (RS19-09); and published Eocene and Oligo-Miocene sandstones (DeCelles et al., 2007a; Han et al., 2019), Figure 5b (2-6)) can be explained by a mixture of input from the Muggar Gangri Complex and the Xiabie granite, both in the hanging wall of the Muggar Thrust; the former has wide age distribution from 150-2,500 Ma (Figure 5b (7)), the latter has a 100-130 Ma peak (Figure 3). The zircon U-Pb ages from the granitic clasts of the Lower Muggar (RS17-N1-C4, -C5, -C6) and Upper Muggar unit (RS17-N4-C1), overlap the emplacement age of the Xiabie granite (Figure 3; 120 Ma); southward paleocurrents and gravel facies suggest that the latter was the proximal source for these clasts (DeCelles et al., 2007a).

Han et al. (2019) noted that detrital zircon U-Pb age spectra from Eocene to Miocene sedimentary rocks of the Lunpola and Nima basins and from the two largest internally draining modern rivers of Tibet, the Zhajia Zangbo and Bocang Zangbo (Figure 1b) lack zircon populations (140-240 Ma) typical of the more distally-located Qiangtang Central Uplift (240-200 Ma), Amdo microcontinent (190-160 Ma) and SW Qiangtang terrain (160-140 Ma) (Figure 5b). They therefore concluded that a short transport internal drainage, similar to modern day was established by late Eocene times (~35 Ma). However, a close examination of the zircon U-Pb age spectra show that a component with ages of 140-240 Ma accounts for ~10% of the total zircon population in their Cretaceous to Oligo-Miocene samples (Figure 5b). Whether such a percentage might be a reasonable proportion delivered by a major long distance-transport river is difficult to assess without knowing the geology of the hypothetical catchment area, and such an age population (140-240 Ma) also has been found in the proximal Muggar Gangri complex in the hanging wall of the Muggar Thrust (Figure 5b). Regardless, the relatively strong peak at 100-130 Ma, most-likely derived from the proximal Xiabie granite, suggests dominant local derivation.

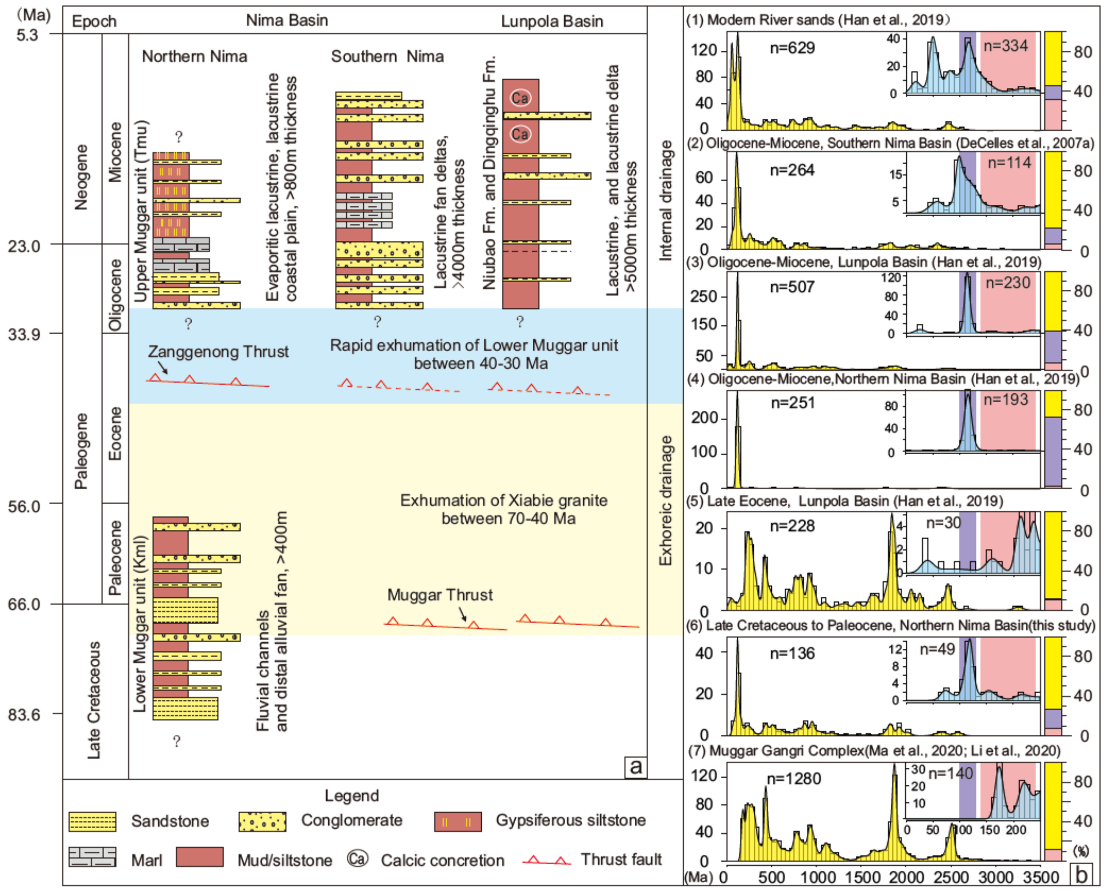

Figure 5. (a) Stratigraphic logs and facies summary from DeCelles et al. (2007a), Han et al. (2019), Fang et al. (2020), showing sampling locations. (b) Kernel density estimation plots with histograms for detrital zircons U-Pb data, including published data where referenced, from modern river sands (plot 1), Cretaceous-Cenozoic sedimentary rocks from the Nima and Lunpola basins (plots 2-6) and the Muggar Thrust hanging wall (plot 7). Purple and pink colors highlight the 100-130 Ma and 140-240 Ma populations, characteristic of the Xiabie granite and more distal regions (see text) respectively. The rectangular boxes to the right show the percentages of populations 100-130 Ma (purple), 140-240 Ma (pink), 0-3500 Ma (yellow).

6.2 The timing and mechanism of exhumation of the Xiabie granite and the Northern Nima Basin

The thermal history of the Early Cretaceous Xiabie granite records a cooling event at 70-40 Ma, with a cooling rate of 3-4°C/Ma (Figure 4c). For an assumed geothermal gradient of 25-30°C/km, this corresponds to a denudation rate of 0.10-0.16 mm/yr. The thermal histories of most of the granitoid and sandstone clasts from the Late Cretaceous Lower Muggar unit reveal a broadly similar pattern: heating to 100 ± 20°C during 70-40 Ma, at a rate of ~3°C/Myr, followed by cooling to 20 ± 10°C at 40-30 Ma, at a cooling rate between 6-8°C/Myr, then a transition to at least one order of magnitude slower cooling (0.25°C-1°C/Myr) at ~30 Ma.

Cooling of a pluton can result from denudation of overlying rocks or heat released during equilibration with the country rock (Mcinnes and Evans, 2005). Cooling of the Xiabie granite at 70-40 Ma has not been previously reported, although Zhao et al. (2020) assumed the existence of this event and used it as a constraint in their thermal modelling based on a regional thermal history (Rohrmann et al., 2012). Provenance studies indicate that the Xiabie granite provided detritus to the Late Cretaceous to Oligocene Lower and Upper Muggar units (DeCelles et al., 2007a), corroborating our hypothesis that the Xiabie granite was exhumed at 70-40 Ma. The 89 Ma AFT age from the Xiabie granite sample RS17-N5 may record early exhumation of the pluton or represent its cooling to the temperature of the country rock (Kapp et al., 2007; Zhao et al., 2020).

The old AFT ages of granite clasts (RS19-10-C1, RS17-N4-C1) from the Upper Muggar unit (67 ± 5 Ma and 51 ± 5 Ma) pre-date the Oligocene stratigraphic age (DeCelles et al., 2007a), suggesting only partial resetting of the fission tracks occurred during burial. The clasts likely retain information on the 70-40 Ma cooling event recorded by the Xiabie granite.

The average AFT age of all granitoid clasts (RS19-06-C3, -C4, -C6, RS17-N1-C4, -C5, -C6) from the Lower Muggar unit are younger than, or overlap, the depositional age, indicating that apatites from these clasts are near-completely annealed. The sandstone clasts (RS17-N1-C1, -N1-C3) failed the chi-square test; RS17-N1-C3 yielded two populations (160 ± 37 Ma, n=6; 58 ± 13 Ma, n=14, respectively), indicating that at least some grains were not completely annealed, whereas the youngest population (58 ± 13 Ma) is, within uncertainty, indistinguishable from the central age of other samples (Figure S5; 53 Ma (RS17-N1-C1) and 50 Ma (RS17-N1-C2)). That the sandstone clasts retained pre-burial signals, whereas the granitoid samples did not, is consistent with a higher average D-par value of the former (Donelick et al., 2005). Both the granite and sandstone clasts show a similar post-depositional thermal history, characterized by moderate heating at ~70-40 Ma, followed by exhumation at 40-30 Ma (Figure 4). This heating event could be due to burial and/or to a magmatic event that drastically increased the geothermal gradient of the basin. However, there are no 70-40 Ma magmatic events reported in the Nima Basin and surrounding areas, and the population of 62~75 Ma zircon U-Pb ages in the sandstone sample (RS19-09) of the Lower Muggar unit is limited (4%; Figure 3). For these reasons we interpret the 70-40 Ma heating of the Lower Muggar unit as predominantly the result of burial, even if a slight increase in the geothermal gradient, due to a blanketing effect of the cover, cannot be discounted (e.g. Luszczak et al., 2017). Cooling can be translated into denudation if the geothermal gradient is known, a value of 30°C/km can be assumed for sedimentary basins. The present geothermal gradient in the nearby Lunpola Basin is around 50°C/km (Liu et al., 2020). Using these two limiting values, Eocene exhumation rates would be 0.27 mm/yr to 0.12 mm/yr.

Given that the climate influence is weak during these times (see section 6.3), we interpret the initiation of the exhumation of the Xiabie granite (70-40 Ma) and the Lower Muggar unit (40-30 Ma) as related to erosion associated with activity of thrust faults in the region. The Xiabie granite is in the hanging wall of the Muggar Thrust; thus we assign the 70-40 Ma exhumation event to tectonic activity of the Muggar Thrust during the latest Cretaceous to early Cenozoic. This is in agreement with the interpretation of Kapp et al. (2007), Rohrmann et al. (2012) and Zhao et al. (2020) for major tectonic activity in the Nima area between 100-40 Ma. The preceding burial stage of the Lower Muggar unit corresponds to the exhumation stage of the Xiabie granite and activity of the Muggar Thrust; we suggest that the latter drove the Lower Muggar unit to subside at 70-40 Ma, allowing the Xiabie granite to be a detrital source for the Lower Muggar unit, which was experiencing burial to 2-4 km. The rapid exhumation at 40-30 Ma of the Lower Muggar unit may be related to movement on the S-dipping Zanggenong Thrusts (Figure 1c), which Kapp et al. (2007) recognized as having deformed the Lower Muggar unit. This interpretation, together with the early Cenozoic activity along the Muggar Thrust, implies that the Nima area was continuously tectonically deformed from ~70 to ~30 Ma. This is in contrast to the existence of a tectonic quiescence period between 50 and 30 Ma proposed by Kapp et al. (2007), and explained as due to preexisting thick crust in southern Tibet was sufficient to inhibit upper-crustal shortening in this area over the period of 50-30 Ma.

The exhumation rate of the Nima area has been very slow since 40-30 Ma. At ~40 Ma, the exhumation rate of the hanging wall decreased by ten-fold (~0.01 mm/yr; Figure 4), while basin inversion in the footwall (0.12-0.27 mm/yr) started, possibly due to movement on the Zanggenong Thrust. No Eocene strata are preserved between the Lower and Upper Muggar units, likely removed by basin exhumation at that time (Figure 5a). By 30 Ma, this exhumation event ceased, as marked by the LTT-derived thermal history and the restart of sedimentation with the deposition of the Upper Muggar unit (Figure 5a). In the last 30 Ma or so, rates of denudation in the Xiabie granite have been low (~0.01 mm/yr) (Figure 4g), and southward-directed palaeocurrents (DeCelles et al., 2007a) suggest that the pluton may have continued to be a source for sediments of the Upper Muggar unit. The lack of annealing in the apatites from the Upper Muggar unit and the LTT-derived thermal history suggest passive exhumation of the hanging wall of the Muggar Thrust throughout the Oligocene (Figure 4).

6.3 Development of internal drainage in the Nima Basin

Several factors influence erosion rates, such as slope, precipitation, glacial cover and tectonic activity (Harrison, 2000; Molnar, 2001; Lal et al., 2004). We interpret that the relatively high rates of denudation of the Xiabie granite at 70-40 Ma and the Northern

Nima Basin at 40-30 Ma was predominantly driven by tectonic activity possibly along the Muggar and Zanggenong thrusts, which led to an increase in relief and river incision. We discount any effect of glacial cover since such an environment has not been recorded in the early Cenozoic in central Tibet. We also consider that any strengthening of precipitation is not the most likely cause for the increase in denudation rates; whilst we acknowledge that there is considerable debate surrounding the climate of the region in the Paleogene (e.g. DeCelles et al., 2007a, 2007b; Su et al., 2019; Fang et al., 2020), we adopt the sedimentological arguments of DeCelles et al. (2007a) since they apply directly to Nima Basin, rather than Lunpola Basin more than 200 km east. DeCelles et al. (2007a) describe sedimentology indicative of an arid climate from Late Cretaceous onwards in the Nima Basin as evidenced by the presence of paleosols, calcareous nodules and large eolian dune fields in the Late Cretaceous Lower Muggar unit; restricted evaporitic lakes in the Late Eocene to Oligocene Upper Muggar unit; and the reconstructed paleogeography and deposystems since Late Cretaceous which are similar to those of the modern arid plateau interior (DeCelles et al., 2007a).

We propose that the evidence for tectonic uplift and consequent erosion in the Muggar thrust hanging wall (Xiabie granite), and subsidence and inversion of the Northern Nima Basin in the footwall, suggest that over the interval of 70-30 Ma, landscape evolution was driven by tectonic events and, in particular, by compressive deformation along the Muggar and Zanggenong thrusts. These deformation events may have led to the establishment of internal drainage in the Nima area. Several lines of stratigraphic and sedimentological evidence support the contention that the Nima area developed internal drainage by 40-30 Ma:

The early Eocene sedimentary record of the Nima area is discontinuous, a consequence of sediment removal during uplift. Section 3MK (Figure 2) records the loss of at least 2 km of section (required to have reset the AHe system and almost completely anneal the tracks in the apatites of the Lower Muggar Unit) suggesting the persistence of an exoreic system in the early Eocene, capable of transporting away the material previously deposited in the Nima Basin. A Late Cretaceous relatively energetic transport environment in the area of the Nima Basin is also evidenced by the sedimentology of the Lower Muggar unit, which is characterized by gravel-dominated fluvial channel and distal alluvial fan deposits (DeCelles et al., 2007a). Following the exhumation of the sedimentary basin, the environmental conditions drastically changed (Figure 5a). The Oligocene Upper Muggar unit is characterized by deposition of massive red gypsiferous siltstone, previously interpreted as shallow, restricted evaporitic lakes, and fluvial systems flowing over a lacustrine coastal plain (DeCelles et al., 2007a). The presence of such massive evaporites and gypsiferous siltstone generally indicate the persistence of an internal drainage system and arid conditions (Langbein, 1961; Vandervoort et al., 1995).

We suggest that the deformation events we document, drove the transformation of the Nima Basin from an exorheic to an endorheic basin by the late Eocene to early Oligocene.

6.4 Implications for the development of Low Relief Topography

Numerous studies have shown that the formation of internal drainage can play an important role in the development of low relief landforms in plateau interiors, such as in Tibet and in the Andes (e.g. Metivier et al. 1998; Garcia-Castellanos, 2007; Liu-Zeng et al., 2008; Strecker et al., 2009). The evolution of an intra-mountain internal drainage traps the eroded material from the orogenic belt in a depression, forming a low-lying plateau landform through a mechanism called “bathtub filling” (Meyer et al. 1998). This process may have occurred in the Nima area, when after ~30 Ma, slow exhumation and the development of an internal drainage system could have promoted the formation of a low relief landscape that is similar to the present day (Lal et al., 2004).

However, we note that other regions have similar deformation and exhumations histories to the Nima Basin and are externally drained. For example, the Fenghuoshan Group of the Hoh Xil Basin was deposited at 75-51 Ma prior to basin inversion at 50-27 Ma (Staisch et al., 2014; 2016). This may suggest that instead of internal drainage development being closely linked to low relief topography, it is onset of tectonic quiescence, in concert with the development of an arid climate, that is the more major influence on the development of low relief topography (Fielding et al., 1994). In the Nima Basin, the thermal histories clearly indicate that around 40 Ma, the exhumation rate decreased in the hanging wall and by 30 Ma regional erosion rates in the basin were low (0.01-0.04 mm/yr). Such low rates imply a low river erosion capacity and, given that the climate remained dry over this interval (DeCelles et al., 2007b), it suggests that the cause of the decreasing exhumation rate is slowing of local tectonic activity.

The extent to which these events can be applied more widely across the region is debatable. The topographic surface expression of the 40-30 Ma thrust activity along the Zanggenong Thrust, which we propose may have resulted in the change from external to internal drainage in the Nima Basin, may be local. Such a proposition is supported firstly by the work of Kapp et al. (2007) who suggested the magnitude of slip on the Zanggenong Thrust is low compared with Cretaceous thrusts. Secondly, magnetostratigraphic studies indicate that the Lunpola Basin experienced relatively slow subsidence (100 m/Ma) from 40 Ma to 25 Ma, suggesting that deformation was limited (Fang et al., 2020, but note the debate on the depositional age dating of this basin in Su et al., 2019). Thirdly, Rohrmann et al. (2012) suggested that the limited number of cooling ages less than 40 Ma in central Tibet be attributed to localized thrust reactivation.

Unlike the Zanggenong Thrust which is a localized feature, the Muggar Thrust is part of the major 1200 km long Shiquanhe-Gaize-Amdo thrust system (Yin and Harrison, 2000). The cessation of activity in the Nima area at 40 Ma is in agreement with the regional synthesis of Rohrmann et al. (2012) and also with our own regional compilation of such LTT data (Figure 1a) which indicates that the central part of the plateau experienced little exhumation and tectonic quiescence since this time. In summary, we suggest that the formation mechanism of low relief topography of central Tibet may be closely related to the extensive tectonic quiescence, the persistence of an arid climate and/or the establishment of internal drainage since ~40-30 Ma. Such a suggestion is in agreement with the observation of Law and Allen (2020) who determined that of low relief topography occurred soon after cessation of exhumation in northern and central Tibet.

7 Conclusions

The Muggar Thrust, part of the 1200 kms long Shiquanhe-Gaize-Amdo thrust system along the Bangong-Nujiang Suture Zone, experienced an exhumational event between 70-40 Ma in the Nima area. Reactivation of local thrusts in the adjacent Nima Basin to the south occurred between 40-30 Ma, after which time exhumation in the region slowed. Consistent with the localized provenance and restricted facies in the Nima Basin, we propose that the thrust-generated topographic expression of relief triggered initiation of internal drainage by ~30 Ma, with subsequent basinal aggradation and development of low relief topography.

Acknowledgements

This work benefited from discussions with Guangwei Li, Peter Molnar, Peter DeCelles, Paul Kapp, Mark Wildman, Jay Quade, Lon Abbott and Ed Sobel. We thank Luigia Di Nicola, Mark Wildman and Jialong Wang for their help in apatite/zircon (U-Th)/He and fission track analysis. We are grateful to editor Taylor Schildgen for efficient handling. The paper benefitted from reviews by Lydia Staisch, Gilby Jepson, Lin Li and associate editor Alexis Ault. This work was financially supported by a

Royal Society Newton Advanced Fellowship (NA160334) and International Exchanges Scheme of the National Natural Science Foundation of China [41761130076] awarded to XH and YN, the Second Tibetan Plateau Scientific Expedition and Research Program, Ministry of Science and Technology, China (2019QZKK0204) awarded to XH, and by the program B for Outstanding PhD candidate of Nanjing University, awarded to WX.

Data Availability Statement

Supporting texts, figures, tables and datasets (Text S1, Figure S1-S6 and Table S1-S6) are provided in Supplementary materials 1 and 2, which can be found at the figshare (https://doi.org/10.6084/m9.figshare.14995134).

References

Andersen, T. (2002). Correction of common lead in U–Pb analyses that do not report 204Pb. *Chemical Geology*, *192*(1), 59-79. https://doi.org/10.1016/S0009-2541(02)00195-X.

Ault, A. K., Flowers, R. M., & Bowring, S. A. (2009). Phanerozoic burial and unroofing history of the western Slave craton and Wopmay orogen from apatite (U–Th)/He thermochronometry. *Earth and Planetary Science Letters*, *284*(1), 1-11. https://doi.org/10.1016/j.epsl.2009.02.035.

Brown, R. W., Beucher, R., Roper, S., Persano, C., Stuart, F., & Fitzgerald, P. (2013). Natural age dispersion arising from the analysis of broken crystals. Part I: Theoretical basis and implications for the apatite (U–Th)/He thermochronometer.

Geochimica et Cosmochimica Acta, *122*, 478-497. https://doi.org/10.1016/j.gca.2013.05.041.

Carlson, W. D., Donelick, R. A., & Ketcham, R. A. (1999). Variability of apatite fission-track annealing kinetics: I. Experimental results. *American Mineralogist*, *84*(9), 1213-1223. https://doi.org/10.2138/am-1999-0901.

Chew, D. M., Babechuk, M. G., Cogné, N., Mark, C., O'Sullivan, G. J., Henrichs, I. A., Doepke, D., & McKenna, C. A. (2016). (LA,Q)-ICPMS trace-element analyses of Durango and McClure Mountain apatite and implications for making natural LA-ICPMS mineral standards. *Chemical Geology*, *435*, 35-48. https://doi.org/10.1016/j.chemgeo.2016.03.028.

Clark, M. K., Royden, L. H., Whipple, K. X., Burchfiel, B. C., Zhang, X., & Tang, W. (2006). Use of a regional, relict landscape to measure vertical deformation of the eastern Tibetan Plateau. *Journal of Geophysical Research: Earth Surface*, *111*(F3). https://doi.org/10.1029/2005JF000294.

Cogné, N., & Gallagher, K. (2021). Some comments on the effect of uranium zonation on fission track dating by LA-ICP-MS. *Chemical Geology*, *573*, 120226. https://doi.org/10.1016/j.chemgeo.2021.120226.

Danišík, M., McInnes, B. I. A., Kirkland, C. L., McDonald, B. J., Evans, N. J., & Becker, T. (2017). Seeing is believing: Visualization of He distribution in zircon and implications for thermal history reconstruction on single crystals. *Science Advances*, *3*(2), e1601121. https://doi.org/doi:10.1126/sciadv.1601121.

DeCelles, P. G., Kapp, P., Ding, L., & Gehrels, G. E. (2007a). Late Cretaceous to middle Tertiary basin evolution in the central Tibetan Plateau: Changing environments in response to tectonic partitioning, aridification, and regional elevation gain. *GSA Bulletin*, *119*(5-6), 654-680. https://doi.org/10.1130/b26074.1.

DeCelles, P. G., Quade, J., Kapp, P., Fan, M., Dettman, D. L., & Ding, L. (2007b). High and dry in central Tibet during the Late Oligocene. *Earth and Planetary Science Letters*, *253*(3), 389-401. https://doi.org/10.1016/j.epsl.2006.11.001.

DeCelles, P. G., Kapp, P., Gehrels, G. E., & Ding, L. (2014). Paleocene-Eocene foreland basin evolution in the Himalaya of southern Tibet and Nepal: Implications for the age of initial India-Asia collision. *Tectonics*, *33*(5), 824-849. https://doi.org/10.1002/2014TC003522.

Deng, L., & Jia, G. (2018). High-relief topography of the Nima basin in central Tibetan Plateau during the mid-Cenozoic time. *Chemical Geology*, *493*, 199-209. https://doi.org/10.1016/j.chemgeo.2018.05.041.

Dewey, J. F., Shackleton, R. M., Chengfa, C., Yiyin, S., Chengfa, C., Shackleton, R. M., Dewey, J. F., & Jixiang, Y. (1988). The tectonic evolution of the Tibetan Plateau. *Philosophical Transactions of the Royal Society of London. Series A, Mathematical and Physical Sciences*, *327*(1594), 379-413. https://doi.org/10.1098/rsta.1988.0135.

Dickinson, W. R., & Gehrels, G. E. (2009). Use of U–Pb ages of detrital zircons to infer maximum depositional ages of strata: A test against a Colorado Plateau Mesozoic database. *Earth and Planetary Science Letters*, *288*(1), 115-125.

https://doi.org/10.1016/j.epsl.2009.09.013.

Ding, L., Qasim, M., Jadoon, I. A. K., Khan, M. A., Xu, Q., Cai, F., Wang, H., Baral, U., & Yue, Y. (2016). The India–Asia collision in north Pakistan: Insight from the U–Pb detrital zircon provenance of Cenozoic foreland basin. *Earth and Planetary Science Letters*, *455*, 49-61. https://doi.org/10.1016/j.epsl.2016.09.003.

Dobson, K. J., Stuart, F. M., & Dempster, T. J. (2008). U and Th zonation in Fish Canyon Tuff zircons: Implications for a zircon (U–Th)/He standard. *Geochimica et Cosmochimica Acta*, *72*(19), 4745-4755. https://doi.org/10.1016/j.gca.2008.07.015.

Donelick, R. A., O'Sullivan, P. B., & Ketcham, R. A. (2005). Apatite Fission-Track Analysis. *Reviews in Mineralogy and Geochemistry*, *58*(1), 49-94. https://doi.org/10.2138/rmg.2005.58.3.

Fang, X., Dupont-Nivet, G., Wang, C., Song, C., Meng, Q., Zhang, W., Nie, J., Zhang, T., Mao, Z., & Chen, Y. (2020). Revised chronology of central Tibet uplift (Lunpola Basin). *Science Advances*, *6*(50), eaba7298. https://doi.org/10.1126/sciadv.aba7298.

Farley, K. A. (2000). Helium diffusion from apatite: General behavior as illustrated by Durango fluorapatite. *Journal of Geophysical Research: Solid Earth*, *105*(B2), 2903-2914. https://doi.org/10.1029/1999JB900348.

Farley, K. A. (2002). (U-Th)/He Dating: Techniques, Calibrations, and Applications. *Reviews in Mineralogy and Geochemistry*, *47*(1), 819-844.

10.2138/rmg.2002.47.18.

Farley, K. A., Wolf, R. A., & Silver, L. T. (1996). The effects of long alpha-stopping distances on (U□Th)/He ages. *Geochimica et Cosmochimica Acta*, *60*(21), 4223-4229. https://doi.org/10.1016/S0016-7037(96)00193-7.

Fernie, N., Glorie, S., Jessell, M. W., & Collins, A. S. (2018). Thermochronological insights into reactivation of a continental shear zone in response to Equatorial Atlantic rifting (northern Ghana). *Scientific Reports*, *8*(1), 16619. https://doi.org/10.1038/s41598-018-34769-x.

Fielding, E., Isacks, B., Barazangi, M., & Duncan, C. (1994). How flat is Tibet? *Geology*, *22*(2), 163-167. https://doi.org/10.1130/0091-7613(1994)022<0163:Hfit>2.3.Co;2.

Flowers, R. M., & Kelley, S. A. (2011). Interpreting data dispersion and “inverted” dates in apatite (U–Th)/He and fission-track datasets: An example from the US midcontinent. *Geochimica et Cosmochimica Acta*, *75*(18), 5169-5186. https://doi.org/10.1016/j.gca.2011.06.016.

Flowers, R. M., Farley, K. A., & Ketcham, R. A. (2015). A reporting protocol for thermochronologic modeling illustrated with data from the Grand Canyon. *Earth and Planetary Science Letters*, *432*, 425-435. https://doi.org/10.1016/j.epsl.2015.09.053.

Flowers, R. M., Ketcham, R. A., Shuster, D. L., & Farley, K. A. (2009). Apatite (U–Th)/He thermochronometry using a radiation damage accumulation and annealing model. *Geochimica et Cosmochimica Acta*, *73*(8), 2347-2365.

https://doi.org/10.1016/j.gca.2009.01.015.

Foeken, J. P. T., Stuart, F. M., Dobson, K. J., Persano, C., & Vilbert, D. (2006). A diode laser system for heating minerals for (U-Th)/He chronometry. *Geochemistry, Geophysics, Geosystems*, *7*(4). https://doi.org/10.1029/2005gc001190.

Fox, M., & Carter, A. (2020). How continuous are the “Relict” landscapes of Southeastern Tibet? *Frontiers in Earth Science*, *8*(587597).

Gallagher, K. (2012). Transdimensional inverse thermal history modeling for quantitative thermochronology. *Journal of Geophysical Research: Solid Earth*, *117*(B2). https://doi.org/10.1029/2011JB008825.

Garcia-Castellanos, D. (2007). The role of climate during high plateau formation. Insights from numerical experiments. *Earth and Planetary Science Letters*, *257*(3), 372-390. https://doi.org/10.1016/j.epsl.2007.02.039.

Gautheron, C., Tassan-Got, L., Barbarand, J., & Pagel, M. (2009). Effect of alpha-damage annealing on apatite (U–Th)/He thermochronology. *Chemical Geology*, *266*(3), 157-170. https://doi.org/10.1016/j.chemgeo.2009.06.001.

Girardeau, J., Marcoux, J., Allègre, C. J., Bassoullet, J. P., Youking, T., Xuchang, X., Yougong, Z., & Xibin, W. (1984). Tectonic environment and geodynamic significance of the Neo-Cimmerian Donqiao ophiolite, Bangong-Nujiang suture zone, Tibet. *Nature*, *307*(5946), 27-31. https://doi.org/10.1038/307027a0.

Griffin, W. (2008). GLITTER: data reduction software for laser ablation ICP-MS. *Laser Ablation ICP-MS in the Earth Sciences: Current practices and outstanding* *issues*, 308-311.

Guenthner, W. R., Reiners, P. W., & Tian, Y. (2014). Interpreting date–eU correlations in zircon (U-Th)/He datasets: A case study from the Longmen Shan, China. *Earth and Planetary Science Letters, 403,* 328-339. https://doi.org/10.1016/j.epsl.2014.06.050.

Guenthner, W. R., Reiners, P. W., Ketcham, R. A., Nasdala, L., & Giester, G. (2013). Helium diffusion in natural zircon: Radiation damage, anisotropy, and the interpretation of zircon (U-Th)/He thermochronology. *American Journal of Science*, *313*(3), 145-198. https://doi.org/10.2475/03.2013.01.

Han, Z., Sinclair, H. D., Li, Y., Wang, C., Tao, Z., Qian, X., Ning, Z., Zhang, J., Wen, Y., Lin, J., Zhang, B., Xu, M., Dai, J., Zhou, A., Liang, H., & Cao, S. (2019). Internal Drainage Has Sustained Low-Relief Tibetan Landscapes Since the Early Miocene. *Geophysical Research Letters*, *46*(15), 8741-8752. https://doi.org/10.1029/2019GL083019.

Harrison, C. G. A. (2000). What factors control mechanical erosion rates? *International Journal of Earth Sciences*, *88*(4), 752-763. https://doi.org/10.1007/s005310050303.

Hetzel, R., Dunkl, I., Haider, V., Strobl, M., von Eynatten, H., Ding, L., & Frei, D. (2011). Peneplain formation in southern Tibet predates the India-Asia collision and plateau uplift. *Geology*, *39*(10), 983-986. https://doi.org/10.1130/g32069.1.

Hu, X., Garzanti, E., Wang, J., Huang, W., An, W., & Webb, A. (2016). The timing of India-Asia collision onset – Facts, theories, controversies. *Earth-Science Reviews,* *160*, 264-299. https://doi.org/10.1016/j.earscirev.2016.07.014.

Jackson, S. E., Pearson, N. J., Griffin, W. L., & Belousova, E. A. (2004). The application of laser ablation-inductively coupled plasma-mass spectrometry to in situ U–Pb zircon geochronology. *Chemical Geology*, *211*(1), 47-69. https://doi.org/10.1016/j.chemgeo.2004.06.017.

Kapp, P., Yin, A., Harrison, T. M., & Ding, L. (2005). Cretaceous-Tertiary shortening, basin development, and volcanism in central Tibet. *GSA Bulletin*, *117*(7-8), 865-878. https://doi.org/10.1130/b25595.1.

Kapp, P., DeCelles, P. G., Gehrels, G. E., Heizler, M., & Ding, L. (2007). Geological records of the Lhasa-Qiangtang and Indo-Asian collisions in the Nima area of central Tibet. *GSA Bulletin*, *119*(7-8), 917-933. https://doi.org/10.1130/b26033.1.

Kapp, P., Murphy, M. A., Yin, A., Harrison, T. M., Ding, L., & Guo, J. (2003). Mesozoic and Cenozoic tectonic evolution of the Shiquanhe area of western Tibet. *Tectonics*, *22*(4). https://doi.org/10.1029/2001TC001332.

Ketcham, R. A., Carter, A., Donelick, R. A., Barbarand, J., & Hurford, A. J. (2007). Improved modeling of fission-track annealing in apatite. *American Mineralogist*, *92*(5-6), 799-810. https://doi.org/10.2138/am.2007.2281.

Ketcham, R. A., van der Beek, P., Barbarand, J., Bernet, M., & Gautheron, C. (2018). Reproducibility of Thermal History Reconstruction From Apatite Fission-Track and (U-Th)/He Data. *Geochemistry, Geophysics, Geosystems*, *19*(8), 2411-2436. https://doi.org/10.1029/2018GC007555.

Kong, X., Mi, W., Zhu, L., & Yang, W. (2019). Zircon U-Pb chronology and provenance of the Paleogene sandstones in the Nima basin, Tibet: implication for coeval paleogeography. *Arabian Journal of Geosciences, 12*(22), https://doi.org/692. 10.1007/s12517-019-4821-2.

Lal, D., Harris, N. B. W., Sharma, K. K., Gu, Z., Ding, L., Liu, T., Dong, W., Caffee, M. W., & Jull, A. J. T. (2004). Erosion history of the Tibetan Plateau since the last interglacial: constraints from the first studies of cosmogenic ^{10}Be from Tibetan bedrock. *Earth and Planetary Science Letters, 217*(1), 33-42. https://doi.org/10.1016/S0012-821X(03)00600-9.

Langbein, W. B. (1961), *Salinity and hydrology of closed lakes: A study of the long-term balance between input and loss of salts in closed lakes*, US GovernmentPrint. Office.

Law, R., & Allen, M. B. (2020). Diachronous Tibetan Plateau landscape evolution derived from lava field geomorphology. *Geology*, *48*(3), 263-267. https://doi.org/10.1130/g47196.1.

Li, C., Wang, G. H., Zhao, Z. B., Du, J. X., Ma, X. X., & Zheng, Y. L. (2020). Late Mesozoic tectonic evolution of the central Bangong–Nujiang Suture Zone, central Tibetan Plateau. *International Geology Review*, *62*(18), 2300-2323. https://doi.org/10.1080/00206814.2019.1697859.

Li, G., Kohn, B., Sandiford, M., Xu, Z., Tian, Y., & Seiler, C. (2016). Synorogenic morphotectonic evolution of the Gangdese batholith, South Tibet: Insights from low-temperature thermochronology. *Geochemistry, Geophysics, Geosystems, 17*(1), 101-112. https://doi.org/10.1002/2015gc006047.

Li, S., Yin, C., Guilmette, C., Ding, L., & Zhang, J. (2019). Birth and demise of the Bangong-Nujiang Tethyan Ocean: A review from the Gerze area of central Tibet. *Earth-Science Reviews*, *198*, 102907. https://doi.org/10.1016/j.earscirev.2019.102907.

Liu-Zeng, J., Tapponnier, P., Gaudemer, Y., & Ding, L. (2008). Quantifying landscape differences across the Tibetan plateau: Implications for topographic relief evolution. *Journal of Geophysical Research: Earth Surface*, *113*(F4). https://doi.org/10.1029/2007JF000897.

Liu, Y., Ye, J., Cao, Q., Yang, B., & Liu, Z. (2020). Hydrocarbon Generation, Migration, and Accumulation in the Eocene Niubao Formation in the Lunpola Basin, Tibet, China: Insights from Basin Modeling and Fluid Inclusion Analysis. *Journal of Earth Science*, *31*(1), 195-206. https://doi.org/10.1007/s12583-019-1211-3.

Liu, Y., Hu, Z., Zong, K., Gao, C., Gao, S., Xu, J., & Chen, H. (2010). Reappraisement and refinement of zircon U-Pb isotope and trace element analyses by LA-ICP-MS. *Chinese Science Bulletin*, *55*(15), 1535-1546. https://doi.org/10.1007/s11434-010-3052-4.

Łuszczak, K., Persano, C., Braun, J., & Stuart, F. M. (2017). How local crustal thermal properties influence the amount of denudation derived from low-temperature thermochronometry. *Geology*, *45*(9), 779-782. https://doi.org/10.1130/g39036.1.

Ma, A., Hu, X., Kapp, P., Lai, W., Han, Z., & Xue, W. (2020). Mesozoic Subduction

Accretion History in Central Tibet Constrained From Provenance Analysis of the Mugagangri Subduction Complex in the Bangong-Nujiang Suture Zone. *Tectonics, 39*(9), e2020TC006144. https://doi.org/10.1029/2020TC006144.

McDannell, K. T., Issler, D. R., & O'Sullivan, P. B. (2019). Radiation-enhanced fission track annealing revisited and consequences for apatite thermochronometry. *Geochimica et Cosmochimica Acta*, *252*, 213-239. https://doi.org/10.1016/j.gca.2019.03.006.

McInnes, B. I. A., Evans, N. J., Fu, F. Q., & Garwin, S. (2005). Application of Thermochronology to Hydrothermal Ore Deposits. *Reviews in Mineralogy and Geochemistry*, *58*(1), 467-498. https://doi.org/10.2138/rmg.2005.58.18.

McKenzie, D., & Jackson, J. (2002). Conditions for flow in the continental crust. *Tectonics*, *21*(6), 5-1-5-7. https://doi.org/10.1029/2002TC001394.

Meng, J., Coe, R. S., Wang, C., Gilder, S. A., Zhao, X., Liu, H., Li, Y., Ma, P., Shi, K., & Li, S. (2017). Reduced convergence within the Tibetan Plateau by 26 Ma? *Geophysical Research Letters*, *44*(13), 6624-6632. https://doi.org/10.1002/2017GL074219.

Métivier, F., Gaudemer, Y., Tapponnier, P., & Meyer, B. (1998). Northeastward growth of the Tibet plateau deduced from balanced reconstruction of two depositional areas: The Qaidam and Hexi Corridor basins, China. *Tectonics*, *17*(6), 823-842. https://doi.org/10.1029/98TC02764.

Meyer, B., Tapponnier, P., Bourjot, L., Métivier, F., Gaudemer, Y., Peltzer, G., Shunmin, G., & Zhitai, C. (1998). Crustal thickening in Gansu-Qinghai, lithospheric mantle subduction, and oblique, strike-slip controlled growth of the Tibet plateau. *Geophysical Journal International*, *135*(1), 1-47. https://doi.org/10.1046/j.1365-246X.1998.00567.x.

Molnar, P. (2001). Climate change, flooding in arid environments, and erosion rates. *Geology*, *29*(12), 1071-1074. https://doi.org/10.1130/0091-7613(2001)029<1071:Ccfiae>2.0.Co;2.

Murphy, M. A., Yin, A., Harrison, T. M., Dürr, S. B., Chen, Z., Ryerson, F. J., Kidd, W. S. F., Wang X., & Zhou, X. (1997). Did the Indo-Asian collision alone create the Tibetan plateau? *Geology*, *25*(8), 719-722. https://doi.org/10.1130/0091-7613(1997)025<0719:Dtiaca>2.3.Co;2.

Persano, C. (2003), A combination of apatite fission track and (U-Th)/He thermochronometers to constrain the escarpment evolution in south eastern Australia: a case study of high elevation passive margins, 23 pp, University of Glasgow.

Reiners, P. W., & Farley, K. A. (2001). Influence of crystal size on apatite (U–Th)/He thermochronology: an example from the Bighorn Mountains, Wyoming. *Earth and Planetary Science Letters*, *188*(3), 413-420. https://doi.org/10.1016/S0012-821X(01)00341-7.

Reiners, P. W., Ehlers, T. A., & Zeitler, P. K. (2005), Past, Present, and Future of Thermochronology. Reviews in Mineralogy and Geochemistry, 58(1), 1-18. https://doi.org/10.2138/rmg.2005.58.1.

Reiners, P. W., & Brandon, M. T. (2006). Using Thermochronology to Understand

Orogenic Erosion. *Annual Review of Earth and Planetary Sciences*, *34*(1), 419-466. https://doi.org/10.1146/annurev.earth.34.031405.125202.

Rohrmann, A., Kapp, P., Carrapa, B., Reiners, P. W., Guynn, J., Ding, L., & Heizler, M. (2012). Thermochronologic evidence for plateau formation in central Tibet by 45 Ma. *Geology*, *40*(2), 187-190. https://doi.org/10.1130/g32530.1.

Staisch, L. M., N. A. Niemi, C. Hong, M. K. Clark, D. B. Rowley, and B. Currie (2014),

A Cretaceous-Eocene depositional age for the Fenghuoshan Group, Hoh Xil Basin: Implications for the tectonic evolution of the northern Tibet Plateau. Tectonics, 33, 281–301. https://doi.org/10.1002/2013TC003367.

Staisch, L. M., Niemi, N. A., Clark, M. K., & Chang, H. (2016). Eocene to late Oligocene history of crustal shortening within the Hoh Xil Basin and implications for the uplift history of the northern Tibetan Plateau. *Tectonics*, *35*(4), 862-895. https://doi.org/10.1002/2015tc003972.

Strecker, M. R., Alonso, R., Bookhagen, B., Carrapa, B., Coutand, I., Hain, M. P., Hilley, G. E., Mortimer, E., Schoenbohm, L., & Sobel, E. R. (2009). Does the topographic distribution of the central Andean Puna Plateau result from climatic or geodynamic processes? *Geology*, *37*(7), 643-646. https://doi.org/10.1130/g25545a.1.

Su, T., Farnsworth, A., Spicer, R. A., Huang, J., Wu, F. X., Liu, J., Li, S. F., Xing, Y. W., Huang, Y. J., Deng, W. Y. D., Tang, H., Xu, C. L., Zhao, F., Srivastava, G., Valdes, P. J., Deng, T., & Zhou, Z. K. (2019). No high Tibetan Plateau until the

Neogene. *Science Advances*, *5*(3). https://doi.org/10.1126/sciadv.aav2189.

Institute of Tibetan Geological Survey. (2002a). Geological Report of the 1: 250, 000 Regional Geological Survey in Baingoin Area.

Institute of Tibetan Geological Survey. (2002b). Geological Report of the 1: 250, 000 Regional Geological Survey in Nima Area.

Institute of Tibetan Geological Survey. (2003a). Geological Report of the 1: 250, 000 Regional Geological Survey in Zigetangco Area.

Institute of Tibetan Geological Survey. (2003b). Geological Report of the 1: 250, 000 Regional Geological Survey in Duoba Area.

Institute of Tibetan Geological Survey. (2006a). Geological Report of the 1: 250, 000 Regional Geological Survey in Paduco Area.

Institute of Tibetan Geological Survey. (2006b). Geological Report of the 1: 250, 000 Regional Geological Survey in Angdaerco Area.

Vandervoort, D. S., Jordan, T. E., Zeitler, P. K., & Alonso, R. N. (1995). Chronology of internal drainage development and uplift, southern Puna plateau, Argentine central Andes. *Geology*, *23*(2), 145-148. https://doi.org/10.1130/0091-7613(1995)023<0145:Coidda>2.3.Co;2.

Vermeesch, P. (2018). IsoplotR: A free and open toolbox for geochronology. *Geoscience Frontiers*, *9*(5), 1479-1493. https://doi.org/10.1016/j.gsf.2018.04.001.

Vermeesch, P., Seward, D., Latkoczy, C., Wipf, M., Günther, D., & Baur, H. (2007). α-Emitting mineral inclusions in apatite, their effect on (U–Th)/He ages, and how to reduce it. *Geochimica et Cosmochimica Acta*, *71*(7), 1737-1746. https://doi.org/10.1016/j.gca.2006.09.020.

Volkmer, J. E., Kapp, P., Guynn, J. H., & Lai, Q. (2007). Cretaceous-Tertiary structural evolution of the north central Lhasa terrane, Tibet. *Tectonics*, *26*(6). https://doi.org/10.1029/2005TC001832.

Wang, N., & Wu, F. (2015). New Oligocene cyprinid in the central Tibetan Plateau documents the pre-uplift tropical lowlands. *Ichthyological research*, *62*(3), 274-285. https://doi.org/10.1007/s10228-014-0438-3.

Wiedenbeck, M., Allé, P., Corfu, F., Griffin, W. L., Meier, M., Oberli, F., Quadt, A. V., Roddick, J.C., & Spiegel, W. (1995). THREE NATURAL ZIRCON STANDARDS FOR U-TH-PB, LU-HF, TRACE ELEMENT AND REE ANALYSES. *Geostandards Newsletter*, *19*(1), 1-23. https://doi.org/10.1111/j.1751-908X.1995.tb00147.x.

Wildman, M., Brown, R., Beucher, R., Persano, C., Stuart, F., Gallagher, K., Schwanethal, J., & Carter, A. (2016). The chronology and tectonic style of landscape evolution along the elevated Atlantic continental margin of South Africa resolved by joint apatite fission track and (U-Th-Sm)/He thermochronology. *Tectonics*, *35*(3), 511-545. https://doi.org/10.1002/2015tc004042.

Yang, R., Willett, S. D., & Goren, L. (2015). In situ low-relief landscape formation as a result of river network disruption. *Nature*, *520*(7548), 526-529. https://doi.org/10.1038/nature14354.

Yang, Z. Y., Wang, Q., Yang, J. H., Dan, W., Zhang, X. Z., Ma, L., Qi, Y., Wang, J., & Sun, P. (2019). Petrogenesis of Early Cretaceous granites and associated microgranular enclaves in the Xiabie Co area, central Tibet: Crust-derived magma mixing and melt extraction. *Lithos*, *350-351*, 105199. https://doi.org/10.1016/j.lithos.2019.105199.

Yin, A., & Harrison, T. M. (2000). Geologic Evolution of the Himalayan-Tibetan Orogen. *Annual Review of Earth and Planetary Sciences*, *28*(1), 211-280. https://doi.org/10.1146/annurev.earth.28.1.211.

Yuan, X. P., Huppert, K. L., Braun, J., Shen, X., Liu-Zeng, J., Guerit, L., Wolf, S. G., Zhang, J. F., & Jolivet, M. (2021). Propagating uplift controls on high-elevation, low-relief landscape formation in the southeast Tibetan Plateau. *Geology*. https://doi.org/10.1130/g49022.1.

Zhang, H., Lu, H., Stevens, T., Feng, H., Fu, Y., Geng, J., & Wang, H. (2018). Expansion of Dust Provenance and Aridification of Asia Since ~7.2 Ma Revealed by Detrital Zircon U-Pb Dating. *Geophysical Research Letters*, *45*(24), 13,437-413,448. https://doi.org/10.1029/2018GL079888.

Zhao, Z. B., Bons, P. D., Li, C., Wang, G. H., Ma, X. X., & Li, G. W. (2020). The Cretaceous crustal shortening and thickening of the South Qiangtang Terrane and implications for proto-Tibetan Plateau formation. *Gondwana Research*, *78*, 141-155. https://doi.org/10.1016/j.gr.2019.09.003.

Zhu, D. C., Li, S. M., Cawood, P. A., Wang, Q., Zhao, Z. D., Liu, S. A., & Wang, L. Q. (2016). Assembly of the Lhasa and Qiangtang terranes in central Tibet by divergent double subduction. *Lithos*, *245*, 7-17. https://doi.org/10.1016/j.lithos.2015.06.023.

References From the Supporting Information

Bi, W., Han, Z., Li, Y., Li, C., Wang, C., Zhang, J., Han, J., He, H., Qian, X., Xu, T., & Ma, Z. (2020). Deformation and cooling history of the Central Qiangtang terrane, Tibetan Plateau and its tectonic implications. *International Geology Review*, 1-17. https://doi.org/10.1080/00206814.2020.1795733.

Clark, M. K., House, M. A., Royden, L. H., Whipple, K. X., Burchfiel, B. C., Zhang, X., & Tang, W. (2005). Late Cenozoic uplift of southeastern Tibet. *Geology*, 33(6), 525-528. https://doi.org/10.1130/g21265.1.

Dai, J. G., Fox, M., Shuster, D. L., Hourigan, J., Han, X., Li, Y.-L., & Wang, C. S. (2020). Burial and exhumation of the Hoh Xil Basin, northern Tibetan Plateau: Constraints from detrital (U-Th)/He ages. *Basin Research*, 32(5). https://doi.org/10.1111/bre.12405.

Dai, J., Wang, C., Hourigan, J., & Santosh, M. (2013a). Multi-stage tectono-magmatic events of the Eastern Kunlun Range, northern Tibet: Insights from U–Pb geochronology and (U–Th)/He thermochronology. *Tectonophysics*, 599, 97-106. https://doi.org/10.1016/j.tecto.2013.04.005.

Dai, J., Wang, C., Hourigan, J., & Santosh, M. (2013b). Insights into the early Tibetan Plateau from (U–Th)/He thermochronology. *Journal of the Geological Society*, 170(6), 917-927. https://doi.org/10.1144/jgs2012-076.

Deeken, A., Thiede, R. C., Sobel, E. R., Hourigan, J. K., & Strecker, M. R. (2011). Exhumational variability within the Himalaya of northwest India. *Earth and Planetary Science Letters,* 305(1), 103-114. https://doi.org/10.1016/j.epsl.2011.02.045.

Flowers, R. M., Ketcham, R. A., Shuster, D. L., & Farley, K. A. (2009). Apatite (U–Th)/He thermochronometry using a radiation damage accumulation and annealing model. *Geochimica et Cosmochimica Acta*, 73(8), 2347-2365. https://doi.org/10.1016/j.gca.2009.01.015.

Gallagher, K. (2016). Comment on 'A reporting protocol for thermochronologic modeling illustrated with data from the Grand Canyon' by Flowers, Farley and Ketcham. *Earth and Planetary Science Letters*, 441, 211-212.

Gautheron, C., Tassan-Got, L., Barbarand, J., & Pagel, M. (2009). Effect of alpha-damage annealing on apatite (U–Th)/He thermochronology. *Chemical Geology*, 266(3), 157-170. https://doi.org/10.1016/j.chemgeo.2009.06.001.

Ge, Y., Li, Y., Wang, X., Qian, X., Zhang, J., Zhou, A., & Liu-Zeng, J. (2018). Oligocene-Miocene burial and exhumation of the southernmost Gangdese mountains from sedimentary and thermochronological evidence. *Tectonophysics*, 723, 68-80. https://doi.org/10.1016/j.tecto.2017.12.003.

Gourbet, L., Mahéo, G., Shuster, D. L., Tripathy-Lang, A., Leloup, P. H., & Paquette, J. L. (2016). River network evolution as a major control for orogenic exhumation: Case study from the western Tibetan plateau. *Earth and Planetary Science*

Letters, 456, 168-181. https://doi.org/10.1016/j.epsl.2016.09.037.

Haider, V. L., Dunkl, I., Eynatten, H. v., Ding, L., Frei, D., & Zhang, L. (2013). Cretaceous to Cenozoic evolution of the northern Lhasa Terrane and the Early Paleogene development of peneplains at Nam Co, Tibetan Plateau. *Journal of Asian Earth Sciences*, 70-71, 79-98. https://doi.org/10.1016/j.jseaes.2013.03.005.

Hetzel, R., Dunkl, I., Haider, V., Strobl, M., von Eynatten, H., Ding, L., & Frei, D. (2011). Peneplain formation in southern Tibet predates the India-Asia collision and plateau uplift. *Geology*, 39(10), 983-986. https://doi.org/10.1130/g32069.1.

Jian, X., Guan, P., Zhang, W., Liang, H., Feng, F., & Fu, L. (2018). Late Cretaceous to early Eocene deformation in the northern Tibetan Plateau: Detrital apatite fission track evidence from northern Qaidam basin. *Gondwana Research*, 60, 94-104. https://doi.org/10.1016/j.gr.2018.04.007.

Kirstein, L. A., Sinclair, H., Stuart, F. M., & Dobson, K. (2006). Rapid early Miocene exhumation of the Ladakh batholith, western Himalaya. *Geology*, 34(12), 1049-1052. https://doi.org/10.1130/g22857a.1.

Lee, J., Hager, C., Wallis, S. R., Stockli, D. F., Whitehouse, M. J., Aoya, M., & Wang, Y. (2011). Middle to late Miocene extremely rapid exhumation and thermal reequilibration in the Kung Co rift, southern Tibet. *Tectonics*, 30(2). https://doi.org/10.1029/2010TC002745.

Li, C., Zheng, D., Zhou, R., Yu, J., Wang, Y., Pang, J., Wang, Y., Hao, Y., & Li, Y. (2021). Late Oligocene Tectonic Uplift of the East Kunlun Shan: Expansion of the Northeastern Tibetan Plateau. *Geophysical Research Letters*, 48(3), e2020GL091281. https://doi.org/10.1029/2020GL091281.

Li, G., Kohn, B., Sandiford, M., Xu, Z., & Wei, L. (2015). Constraining the age of Liuqu Conglomerate, southern Tibet: Implications for evolution of the India–Asia collision zone. *Earth and Planetary Science Letters*, 426, 259-266. https://doi.org/10.1016/j.epsl.2015.06.010.

Li, G., Kohn, B., Sandiford, M., Ma, Z., & Xu, Z. (2018). Post-collisional exhumation of the Indus-Yarlung suture zone and Northern Tethyan Himalaya, Saga, SW Tibet. *Gondwana Research*, 64, 1-10. https://doi.org/10.1016/j.gr.2018.06.006.

Li, G., Sandiford, M., Fang, A., Kohn, B., Sandiford, D., Fu, B., Zhang, T., Cao, Y., & Chen, F. (2019). Multi-stage exhumation history of the West Kunlun orogen and the amalgamation of the Tibetan Plateau. *Earth and Planetary Science Letters*, 528, 115833. https://doi.org/10.1016/j.epsl.2019.115833.

Li, H. A., Dai, J.-G., Xu, S.-Y., Liu, B.-R., Han, X., Wang, Y.-N., & Wang, C.-S. (2019). The formation and expansion of the eastern Proto-Tibetan Plateau: Insights from low-temperature thermochronology. *Journal of Asian Earth Sciences*, 183, 103975. https://doi.org/10.1016/j.jseaes.2019.103975.

Liu-Zeng, J., Zhang, J., McPhillips, D., Reiners, P., Wang, W., Pik, R., Zeng, L., Hoke, G., Xie, K., Xiao, P., Zheng, D., & Ge, Y. (2018). Multiple episodes of fast exhumation since Cretaceous in southeast Tibet, revealed by low-temperature thermochronology. *Earth and Planetary Science Letters*, 490, 62-76.

https://doi.org/10.1016/j.epsl.2018.03.011.

Lu, L., Zhen, Z., Zhenhan, W., Cheng, Q., & Peisheng, Y. (2015). Fission Track Thermochronology Evidence for the Cretaceous and Paleogene Tectonic Event of Nyainrong Microcontinent, Tibet. *Acta Geologica Sinica - English Edition*, 89(1), 133-144. https://doi.org/10.1111/1755-6724.12400.

McRivette, M. W., Yin, A., Chen, X., & Gehrels, G. E. (2019). Cenozoic basin evolution of the central Tibetan plateau as constrained by U-Pb detrital zircon geochronology, sandstone petrology, and fission-track thermochronology. *Tectonophysics*, 751, 150-179. https://doi.org/10.1016/j.tecto.2018.12.015.

Meesters, A. G. C. A., & Dunai, T. J. (2002). Solving the production–diffusion equation for finite diffusion domains of various shapes: Part I. Implications for low-temperature (U–Th)/He thermochronology. *Chemical Geology*, 186(3), 333-344. https://doi.org/10.1016/S0009-2541(01)00422-3.

Nie, J., Ruetenik, G., Gallagher, K., Hoke, G., Garzione, C. N., Wang, W., Stockli, D., Hu, X., Wang, Z., Wang, Y., Stevens, T., Danišík, M., & Liu, S. (2018). Rapid incision of the Mekong River in the middle Miocene linked to monsoonal precipitation. *Nature Geoscience*, 11(12), 944-948. https://doi.org/10.1038/s41561-018-0244-z.

Qian, X., Li, Y., Dai, J., Wang, C., Han, Z., Zhang, J., & Li, H. a. (2021). Apatite and zircon (U–Th)/He thermochronological evidence for Mesozoic exhumation of the Central Tibetan Mountain Range. *Geological Journal*, 56(1), 599-611.

https://doi.org/10.1002/gj.3979.

Staisch, L. M., Niemi, N. A., Clark, M. K., & Chang, H. (2016). Eocene to late Oligocene history of crustal shortening within the Hoh Xil Basin and implications for the uplift history of the northern Tibetan Plateau. *Tectonics*, 35(4), 862-895. https://doi.org/10.1002/2015tc003972.

Tian, Y., Kohn, B. P., Hu, S., & Gleadow, A. J. W. (2015). Synchronous fluvial response to surface uplift in the eastern Tibetan Plateau: Implications for crustal dynamics. *Geophysical Research Letters*, 42(1), 29-35. https://doi.org/10.1002/2014GL062383.

van der Beek, P., Van Melle, J., Guillot, S., Pêcher, A., Reiners, P. W., Nicolescu, S., & Latif, M. (2009). Eocene Tibetan plateau remnants preserved in the northwest Himalaya. *Nature Geoscience*, 2(5), 364-368. https://doi.org/10.1038/ngeo503.

Vermeesch, P. (2018). IsoplotR: A free and open toolbox for geochronology. *Geoscience Frontiers*, 9(5), 1479-1493. https://doi.org/10.1016/j.gsf.2018.04.001.

Vermeesch, P., & Tian, Y. (2014). Thermal history modelling: HeFTy vs. QTQt. *Earth-Science Reviews*, 139, 279-290. https://doi.org/10.1016/j.earscirev.2014.09.010.

Wang, E., Kirby, E., Furlong, K. P., van Soest, M., Xu, G., Shi, X., Kamp, P. J. J., & Hodges, K. V. (2012). Two-phase growth of high topography in eastern Tibet during the Cenozoic. *Nature Geoscience*, 5(9), 640-645.

https://doi.org/10.1038/ngeo1538.

Wang, F., Shi, W., Zhang, W., Wu, L., Yang, L., Wang, Y., & Zhu, R. (2017). Differential growth of the northern Tibetan margin: evidence for oblique stepwise rise of the Tibetan Plateau. *Scientific Reports*, 7(1), 41164. https://doi.org/10.1038/srep41164.

Wang, L. C., & Wei, Y. S. (2013). Apatite fission track thermochronology evidence for the Mid-Cretaceous tectonic event in the Qiangtang Basin, Tibet. *Acta Petrologica Sinica*, 29(3), 1039-1047.

Wang, Y., Zhang, X., Sun, L., & Wan, J. (2007). Cooling history and tectonic exhumation stages of the south-central Tibetan Plateau (China): Constrained by 40Ar/39Ar and apatite fission track thermochronology. *Journal of Asian Earth Sciences*, 29(2), 266-282. https://doi.org/10.1016/j.jseaes.2005.11.001.

Yang, H., Song, Y., Tang, J., Wang, Q., Gao, K., & Wei, S. (2020). Low Temperature History of the Tiegelongnan Porphyry–Epithermal Cu (Au) Deposit in the Duolong Ore District of Northwest Tibet, China. *Resource Geology*, 70(2), 111-124. https://doi.org/10.1111/rge.12221.

Zhang, H., Oskin, M. E., Liu-Zeng, J., Zhang, P., Reiners, P. W., & Xiao, P. (2016). Pulsed exhumation of interior eastern Tibet: Implications for relief generation mechanisms and the origin of high-elevation planation surfaces. *Earth and Planetary Science Letters*, 449, 176-185. https://doi.org/10.1016/j.epsl.2016.05.048.

Zhao, Z. B., Bons, P. D., Li, C., Wang, G. H., Ma, X. X., & Li, G. W. (2020). The Cretaceous crustal shortening and thickening of the South Qiangtang Terrane and implications for proto-Tibetan Plateau formation. *Gondwana Research*, 78, 141-155. https://doi.org/10.1016/j.gr.2019.09.003.

Figure 1.

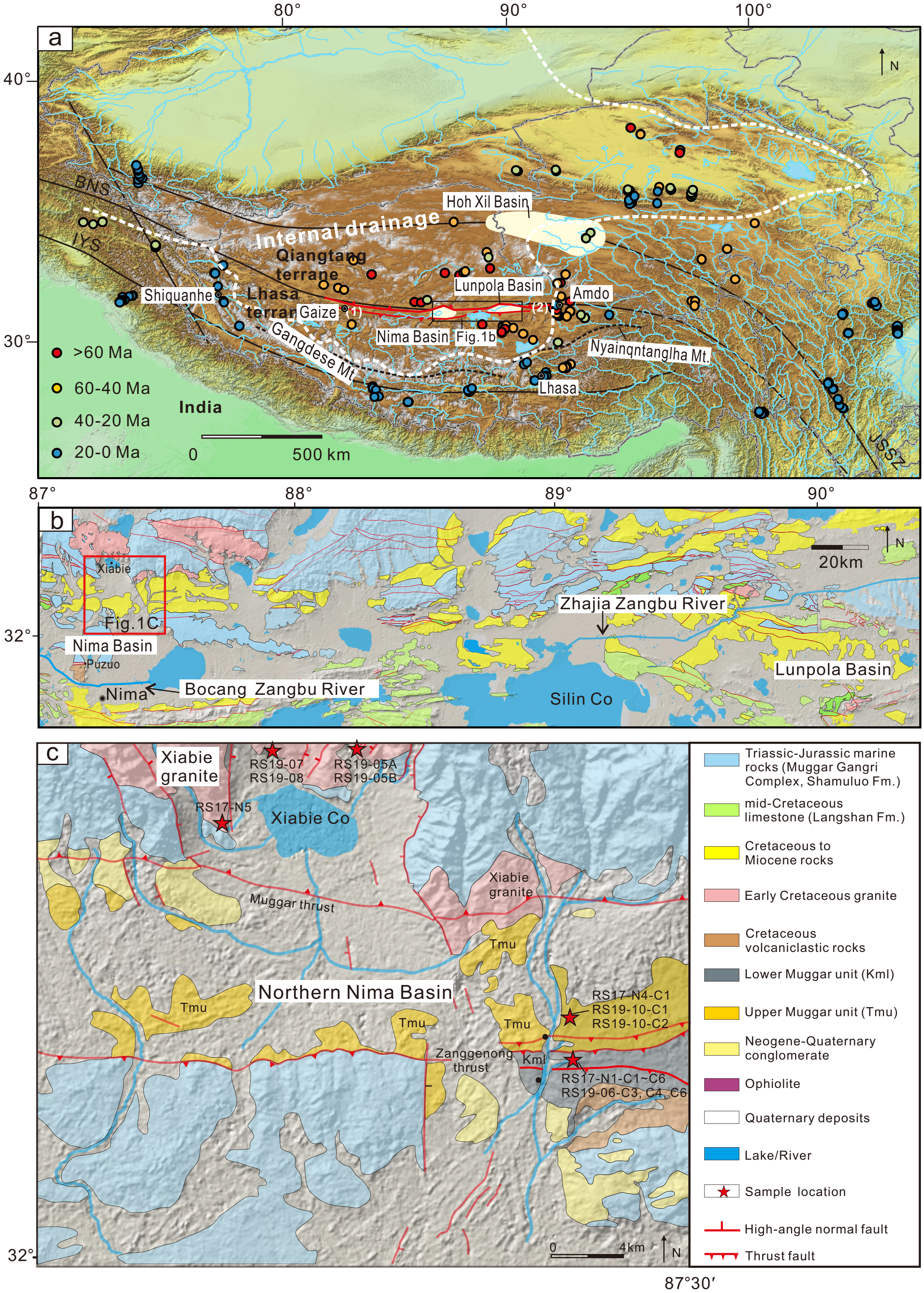

a
80°
90°
100°
40°
30°
N
BNS
IYS
Internal drainage
Hoh Xil Basin
Qiangtang terrane
Lhasa terrane
Shiquanhe
Gaize
Lunpola Basin
Amdo
Nima Basin
Fig.1b
Gangdese Mt.
Nyainqntanglha Mt.
Lhasa
India
JSSZ
>60 Ma
60-40 Ma
40-20 Ma
20-0 Ma
0
500 km
b
87°
88°
89°
90°
32°
Xiabie
Fig.1C
Nima Basin
Puzuo
Nima
Bocang Zangbu River
Zhajia Zangbu River
Silin Co
Lunpola Basin
20km
c
Xiabie granite
RS19-07
RS19-08
RS19-05A
RS19-05B
RS17-N5
Xiabie Co
Xiabie granite
Muggar thrust
Tmu
Northern Nima Basin
RS17-N4-C1
RS19-10-C1
RS19-10-C2
Zanggenong thrust
Kml
RS17-N1-C1~C6
RS19-06-C3, C4, C6
0
4km
32°
87°30′
Triassic-Jurassic marine rocks (Muggar Gangri Complex, Shamuluo Fm.)
mid-Cretaceous limestone (Langshan Fm.)
Cretaceous to Miocene rocks
Early Cretaceous granite
Cretaceous volcaniclastic rocks
Lower Muggar unit (Kml)
Upper Muggar unit (Tmu)
Neogene-Quaternary conglomerate
Ophiolite
Quaternary deposits
Lake/River
Sample location
High-angle normal fault
Thrust fault

Figure 2.

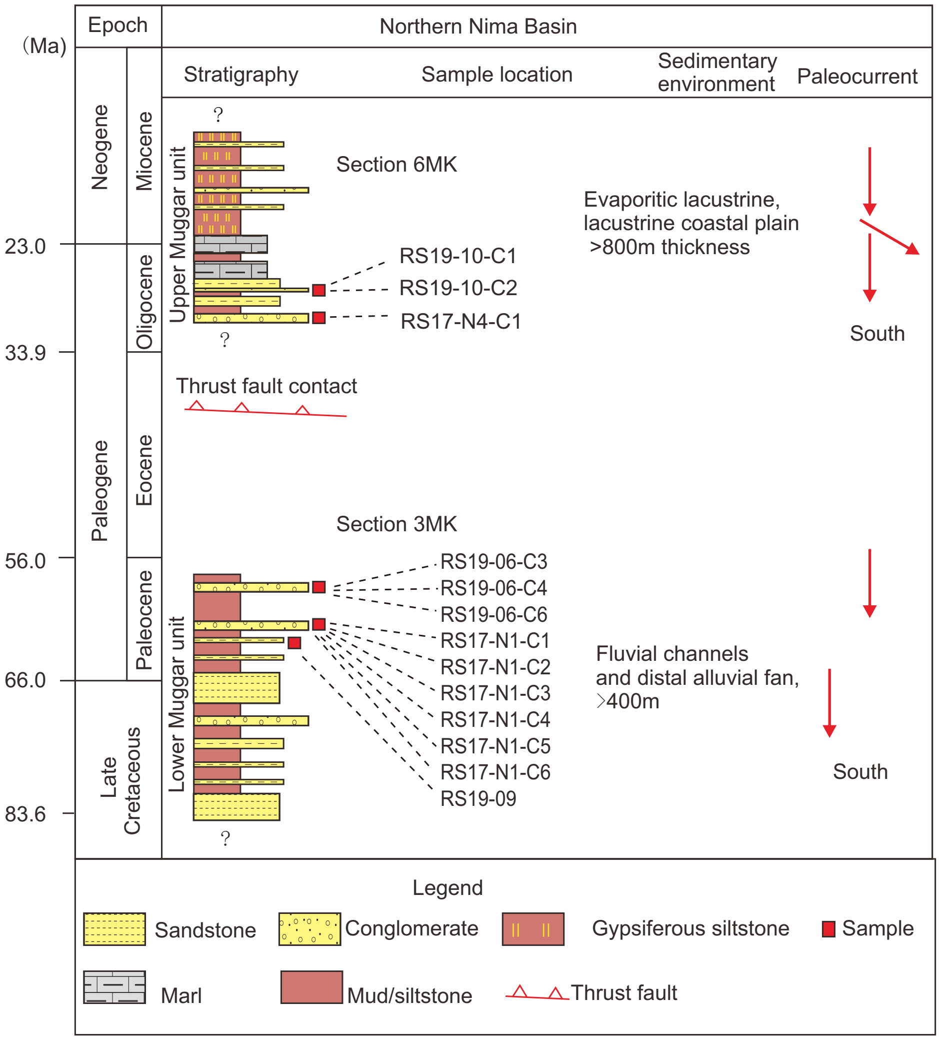

(Ma)
Epoch
Northern Nima Basin
Stratigraphy
Sample location
Sedimentary environment
Paleocurrent
Neogene
Miocene
Paleogene
Oligocene
Eocene
Paleocene
Late Cretaceous
23.0
33.9
56.0
66.0
83.6
Upper Muggar unit
Lower Muggar unit
Section 6MK
RS19-10-C1
RS19-10-C2
RS17-N4-C1
Evaporitic lacustrine, lacustrine coastal plain >800m thickness
South
Thrust fault contact
Section 3MK
RS19-06-C3
RS19-06-C4
RS19-06-C6
RS17-N1-C1
RS17-N1-C2
RS17-N1-C3
RS17-N1-C4
RS17-N1-C5
RS17-N1-C6
RS19-09
Fluvial channels and distal alluvial fan, >400m
South
Legend
Sandstone
Conglomerate
Gypsiferous siltstone
Sample
Marl
Mud/siltstone
Thrust fault

Figure 3.

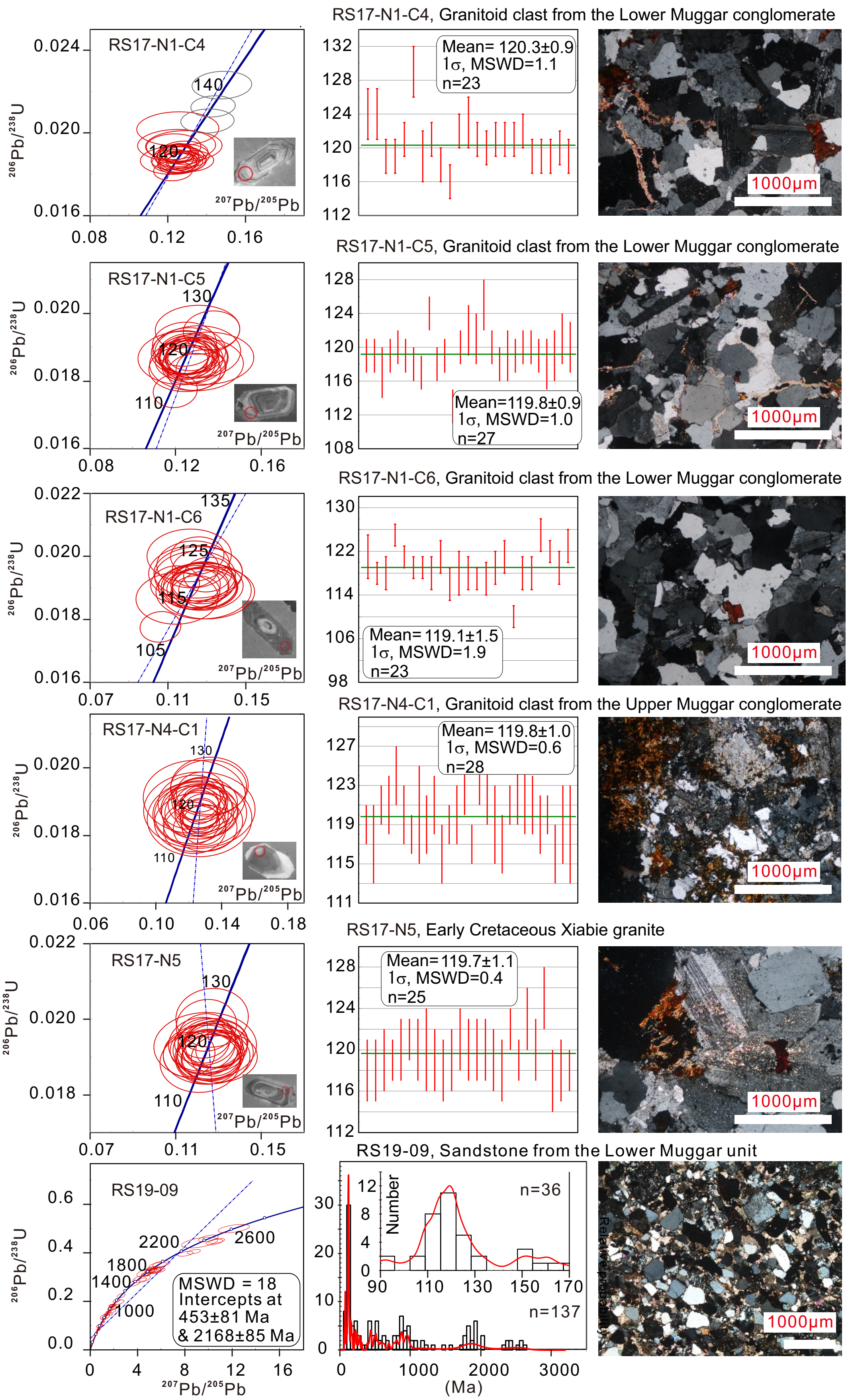
RS17-N1-C4, Granitoid clast from the Lower Muggar conglomerate
RS17-N1-C4
Mean= 120.3±0.9
1σ, MSWD=1.1
n=23
1000μm
RS17-N1-C5, Granitoid clast from the Lower Muggar conglomerate
RS17-N1-C5
Mean=119.8±0.9
1σ, MSWD=1.0
n=27
1000μm
RS17-N1-C6, Granitoid clast from the Lower Muggar conglomerate
RS17-N1-C6
Mean= 119.1±1.5
1σ, MSWD=1.9
n=23
1000μm
RS17-N4-C1, Granitoid clast from the Upper Muggar conglomerate
RS17-N4-C1
Mean= 119.8±1.0
1σ, MSWD=0.6
n=28
1000μm
RS17-N5, Early Cretaceous Xiabie granite
RS17-N5
Mean=119.7±1.1
1σ, MSWD=0.4
n=25
1000μm
RS19-09, Sandstone from the Lower Muggar unit
RS19-09
MSWD = 18
Intercepts at
453±81 Ma
& 2168±85 Ma
n=36
n=137
Number
(Ma)
1000μm
^{206}Pb/^{238}U
^{207}Pb/^{235}Pb

Figure 4.

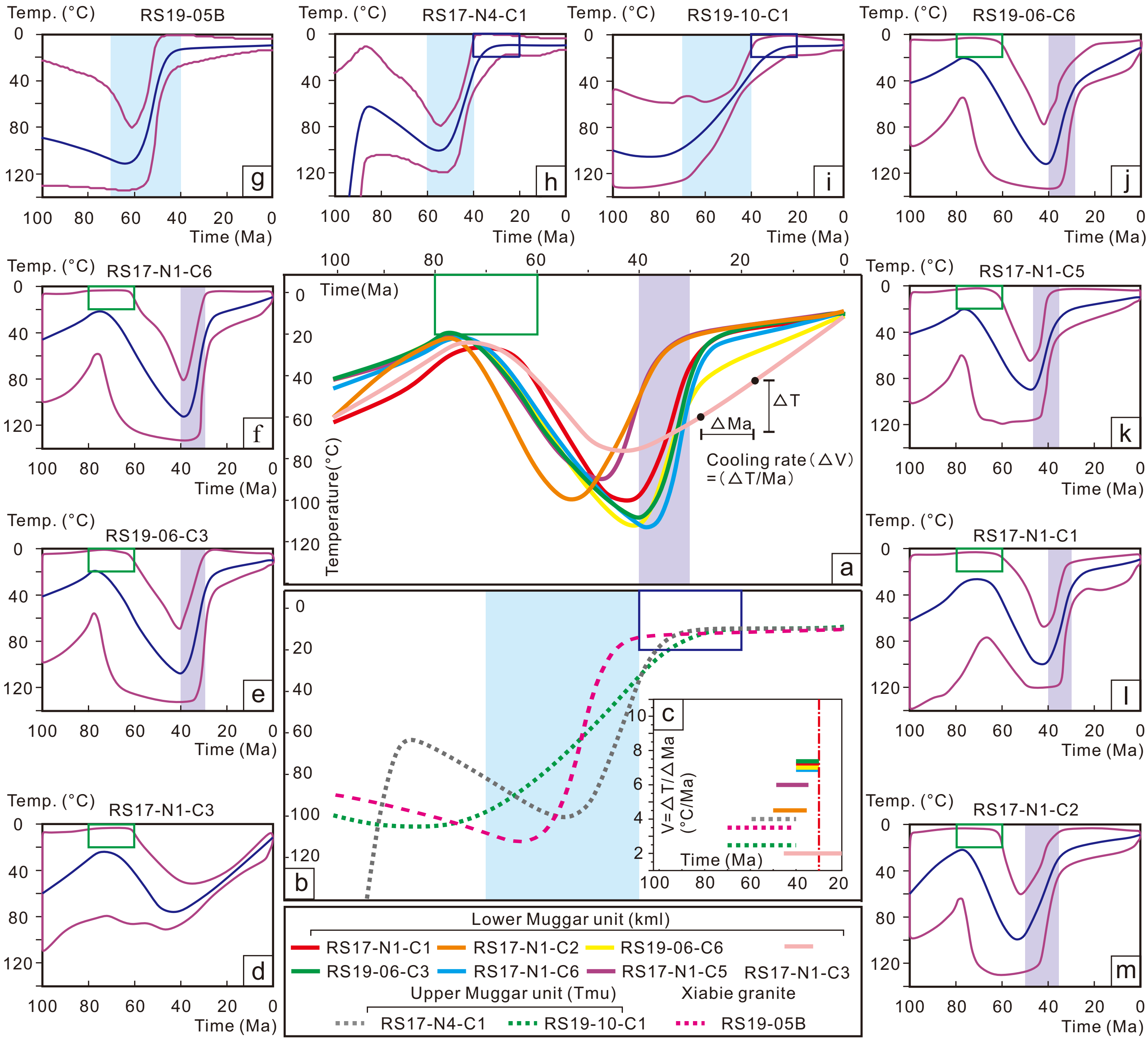

Temp. (°C)
RS19-05B
RS17-N4-C1
RS19-10-C1
RS19-06-C6
RS17-N1-C6
RS17-N1-C5
RS19-06-C3
RS17-N1-C1
RS17-N1-C3
RS17-N1-C2
Time (Ma)
Time(Ma)
Temperature(°C)
△T
△Ma
Cooling rate（△V）
=（△T/Ma）
V=△T/△Ma
(°C/Ma)
Lower Muggar unit (kml)
RS17-N1-C1
RS17-N1-C2
RS19-06-C6
RS19-06-C3
RS17-N1-C6
RS17-N1-C5
RS17-N1-C3
Upper Muggar unit (Tmu)
Xiabie granite
RS17-N4-C1
RS19-10-C1
RS19-05B

Figure 5.

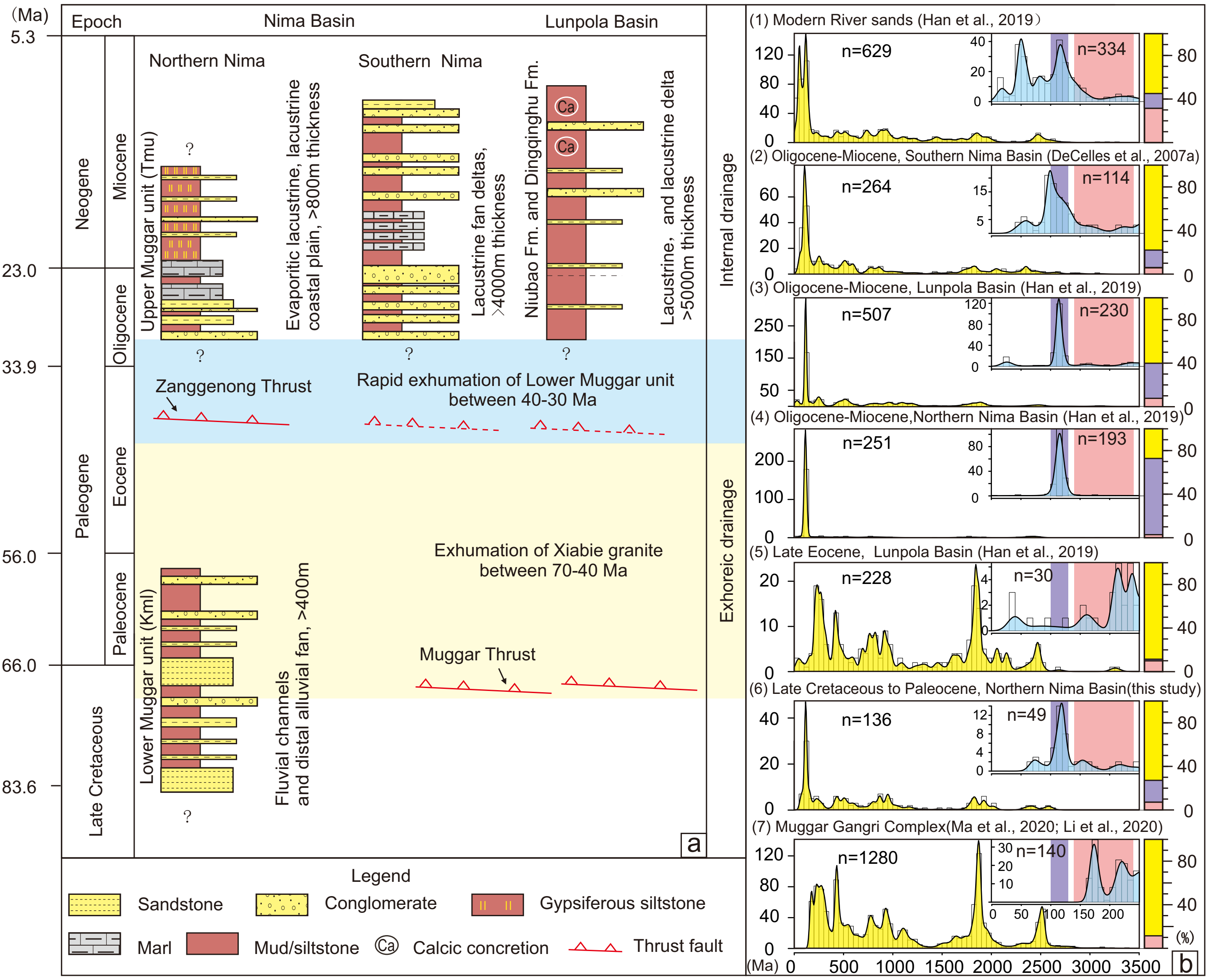

(Ma)
Epoch
Nima Basin
Lunpola Basin
Northern Nima
Southern Nima
Neogene
Miocene
Oligocene
Paleogene
Eocene
Paleocene
Late Cretaceous
5.3
23.0
33.9
56.0
66.0
83.6
Upper Muggar unit (Tmu)
Evaporitic lacustrine, lacustrine coastal plain, >800m thickness
Lacustrine fan deltas, >4000m thickness
Niubao Fm. and Dingqinghu Fm.
Lacustrine, and lacustrine delta >5000m thickness
Zanggenong Thrust
Rapid exhumation of Lower Muggar unit between 40-30 Ma
Exhumation of Xiabie granite between 70-40 Ma
Muggar Thrust
Lower Muggar unit (Kml)
Fluvial channels and distal alluvial fan, >400m
a
Legend
Sandstone
Conglomerate
Gypsiferous siltstone
Marl
Mud/siltstone
Calcic concretion
Thrust fault
Internal drainage
Exhoreic drainage
(1) Modern River sands (Han et al., 2019)
n=629
n=334
(2) Oligocene-Miocene, Southern Nima Basin (DeCelles et al., 2007a)
n=264
n=114
(3) Oligocene-Miocene, Lunpola Basin (Han et al., 2019)
n=507
n=230
(4) Oligocene-Miocene,Northern Nima Basin (Han et al., 2019)
n=251
n=193
(5) Late Eocene, Lunpola Basin (Han et al., 2019)
n=228
n=30
(6) Late Cretaceous to Paleocene, Northern Nima Basin(this study)
n=136
n=49
(7) Muggar Gangri Complex(Ma et al., 2020; Li et al., 2020)
n=1280
n=140
(%)
(Ma) 0 500 1000 1500 2000 2500 3000 3500
b

Table 1 Location, analytical methods employed and lithological details of samples from the Northern Nima Basin and Xiabie granite

Number	Sample	Longitude (°E)	Latitude（°N）	Sample position	Lithology	AFT	AHe	Zircon U-Pb	ZHe
1	RS17-N1-C4	87.4168	32.1014	Lower Muggar Unit	granitoid conglomerate clast	√	√	√	√
2	RS17-N1-C5	87.4168	32.1014	Lower Muggar Unit	granitoid conglomerate clast	√	√	√	√
3	RS17-N1-C6	87.4168	32.1014	Lower Muggar Unit	granitoid conglomerate clast	√	√	√	√
4	RS19-06-C3	87.4171	32.1017	Lower Muggar Unit	granitoid conglomerate clast	√	√		
5	RS19-06-C6	87.4171	32.1017	Lower Muggar Unit	granitoid conglomerate clast	√	√		
6	RS19-06-C4	87.4171	32.1017	Lower Muggar Unit	granitoid conglomerate clast	√	√		
7	RS17-N1-C1	87.4168	32.1014	Lower Muggar Unit	buff sandstone conglomerate clast	√	√		
8	RS17-N1-C2	87.4168	32.1014	Lower Muggar Unit	buff sandstone conglomerate clast	√	√		
9	RS17-N1-C3	87.4168	32.1014	Lower Muggar Unit	buff sandstone conglomerate clast	√	√		
10	RS19-09	87.4171	32.1017	Lower Muggar Unit	sandstone			√	
11	RS17-N4-C1	87.4225	32.1139	Upper Muggar Unit	granitoid conglomerate clast	√	√	√	√
12	RS19-10-C1	87.4210	32.1119	Upper Muggar Unit	granitoid conglomerate clast	√	√		
13	RS19-10-C2	87.4210	32.1119	Upper Muggar Unit	granitoid conglomerate clast		√		
14	RS17-N5	87.2241	32.2186	Xiabie granite	granite	√	√	√	
15	RS19-05B	87.2973	32.2615	Xiabie granite	granite	√	√		
16	RS19-08	87.2694	32.2599	Xiabie granite	granite	√			
17	RS19-07	87.2945	32.2607	Xiabie granite	granite	√			
18	RS19-05A	87.3042	32.2447	Xiabie granite	granite	√			

Note: Tick √ represents the analysis technique carried out for every sample

Table 2. Results of Apatite (U-Th)/He Analysis

Grain name	^{4}He (cc)	^{238}U (ng)	^{232}Th (ng)	eU ppm	[a]T	[b]L (um)	[c]W (um)	Ft	Th/U	Raw age (Ma)	error (Ma)	Cor. Age (Ma)	error (Ma)	Ave. Raw age and SD (Ma)	Ave. Cor. Age And SD (Ma)
RS17-N1-C1-02	2.3E-10	0.019	0.308	28.5	0	120	103	0.7	15.8	20.7	0.8	28.6	1.2		
RS17-N1-C1-03	2.1E-10	0.021	0.229	33.6	0	110	90	0.7	10.7	23.4	0.3	34.1	0.5		
RS17-N1-C1-05	2.8E-10	0.051	0.202	48.2	0	100	90	0.7	4.0	23.7	0.3	34.9	0.4		
RS17-N1-C1-06	2.3E-10	0.037	0.293	26.7	0	130	110	0.7	8.0	17.8	0.2	24.0	0.3		
RS17-N1-C1-07	8.0E-11	0.019	0.244	41.8	0	100	85	0.7	13.1	8.7	0.1	13.0	0.2	/	/
RS17-N1-C2-02	6.0E-11	0.008	0.040	14.3	0	90	73	0.6	5.2	29.1	1.4	47.6	2.2		
RS17-N1-C2-03	8.7E-11	0.015	0.050	16.4	0	100	80	0.7	3.4	27.2	1.0	41.9	1.5		
RS17-N1-C2-04	9.2E-11	0.012	0.087	26.0	0	100	70	0.6	7.4	23.4	0.6	38.1	0.9		
RS17-N1-C2-05	5.2E-11	0.003	0.075	25.4	0	90	60	0.6	23.5	20.8	0.6	37.4	1.1		
RS17-N1-C2-06	9.9E-11	0.035	0.140	94.4	0	80	60	0.5	3.9	11.9	0.4	22.0	0.8	/	/
RS17-N1-C3-01	7.4E-11	0.017	0.131	37.7	0	90	75	0.6	7.6	12.6	0.2	20.3	0.4		
RS17-N1-C3-02	2.7E-11	0.012	0.026	19.4	0	90	65	0.6	2.1	12.0	0.7	20.7	1.2		
RS17-N1-C3-03	4.6E-11	0.018	0.126	23.2	0	100	90	0.7	7.1	8.0	0.1	11.8	0.2		
RS17-N1-C3-04	7.1E-11	0.018	0.081	20.3	0	100	85	0.7	4.5	15.7	0.4	23.7	0.6		
RS17-N1-C3-05	1.7E-10	0.028	0.181	28.2	0	110	95	0.7	6.5	19.4	0.3	27.7	0.4	/	/
RS17-N1-C4-1	1.8E-10	0.012	0.121	48.1	1	110	55	0.5	10.1	35.9	0.5	65.8	0.9		
RS17-N1-C4-2	3.1E-10	0.032	0.170	44.2	1	140	68	0.6	5.3	35.4	0.5	55.8	0.8		
RS17-N1-C4-3	6.6E-10	0.021	0.455	101.0	1	140	60	0.6	21.7	42.2	0.6	70.8	1.0	37.8 ± 3.1	64.2 ± 6.2
RS17-N1-C5-1A	3.7E-10	0.042	0.272	34.4	1	160	88	0.7	6.5	28.7	0.3	40.5	0.5		
RS17-N1-C5-2A	1.5E-10	0.024	0.127	44.7	1	160	55	0.6	5.2	23.1	0.4	40.3	0.7		
RS17-NI-C5-1	3.8E-10	0.046	0.236	24.9	2	200	90	0.7	5.1	30.4	0.4	41.7	0.5		

RS17-NI-C5-3	7.5E-10	0.096	0.354	31.1	1	200	107	0.8	3.7	34.2	0.4	45.1	0.5		
RS17-NI-C5-4	8.5E-10	0.068	0.429	76.0	1	180	70	0.7	6.3	41.5	0.5	63.0	0.7		
RS17-NI-C5-5	6.1E-10	0.106	0.313	14.5	1	300	128	0.8	3.0	28.1	0.3	35.1	0.4	31.0 ± 5.7	44.3 ± 8.8
RS17-N1-C6-2	5.6E-10	0.043	0.375	54.8	2	170	75	0.7	8.6	35.1	0.5	52.0	0.7		
RS17-N1-C6-3	6.3E-10	0.043	0.307	60.3	2	155	70	0.6	7.2	45.1	0.6	69.4	0.9		
RS17-N1-C6-4	3.2E-10	0.066	0.279	59.9	2	155	75	0.7	4.3	20.1	0.2	30.0	0.3		
RS17-N1-C6-2a	1.1E-09	0.108	0.488	157.3	1	137	64	0.6	4.5	41.8	1.0	67.9	1.6		
RS17-N1-C6-3a	3.3E-10	0.033	0.237	49.1	1	140	72	0.6	7.1	30.8	1.5	47.5	2.3		
RS17-N1-C6-4a	3.8E-10	0.028	0.163	44.7	2	140	65	0.6	5.8	46.5	0.7	74.9	1.1		
RS17-N1-C6-6a	5.2E-10	0.098	0.423	72.6	1	150	85	0.7	4.3	21.5	0.2	30.8	0.3	/	/
RS19-06-C3-3	2.8E-10	0.011	0.264	39.0	2	160	68	0.60	23.64	31.62	0.5	52.8	0.8		
RS19-06-C3-5	2.9E-10	0.019	0.242	32.5	2	157	77	0.63	12.78	30.96	0.5	48.8	0.7		
RS19-06-C3-1c	9.6E-11	0.011	0.121	18.3	2	130	81	0.63	10.90	19.94	0.5	31.7	0.8		
RS19-06-C3-2c	1.1E-10	0.014	0.051	11.3	2	157	77	0.65	3.58	35.98	1.6	55.6	2.5		
RS19-06-C3-3c	1.7E-10	0.022	0.075	10.3	2	190	89	0.70	3.46	36.10	1.1	51.7	1.6	30.9 ± 5.9	48.1 ± 8.5
RS19-06-C4-1	6.1E-10	0.058	0.359	21.2	2	210	113	0.74	6.14	34.89	0.3	46.4	0.4		
RS19-06-C4-2	4.8E-10	0.024	0.196	22.4	2	180	83	0.67	8.11	55.50	0.6	82.2	0.8		
RS19-06-C4-3	7.9E-10	0.054	0.209	11.7	2	236	122	0.77	3.87	62.40	0.6	80.5	0.8		
RS19-06-C4-4	9.2E-10	0.099	0.454	42.4	1	232	91	0.73	4.58	36.60	0.3	49.6	0.4	/	/
RS19-06-C6-1	8.4E-11	0.013	0.122	20.2	2	130	80	0.63	9.18	16.10	0.2	26.0	0.3		
RS19-06-C6-2	1.1E-10	0.014	0.076	12.8	2	152	80	0.65	5.54	28.44	0.3	44.5	0.5		
RS19-06-C6-3	2.5E-10	0.026	0.207	29.3	0	163	79	0.65	7.82	27.33	0.3	41.8	0.4		
RS19-06-C6-4	1.3E-10	0.015	0.147	24.4	1	159	72	0.65	9.61	21.28	0.2	32.8	0.4		
RS19-06-C6-5	2.0E-10	0.014	0.166	26.6	1	130	78	0.67	11.49	29.93	0.3	44.3	0.5		
RS19-06-C6-1C	4.4E-10	0.050	0.406	26.7	2	183	109	0.72	8.17	24.78	0.2	34.2	0.3	24.6 ± 4.7	37.3 ± 6.8
RS19-10-C1-1	3.3E-10	0.021	0.341	60.3	2	130	72	0.60	15.96	26.69	0.3	44.9	0.6		

RS19-10-C1-2	2.8E-10	0.011	0.296	56.8	2	123	68	0.57	27.77	28.13	0.4	49.3	0.7		
RS19-10-C1-3	1.8E-10	0.020	0.101	22.8	2	160	69	0.62	4.98	32.71	0.8	52.8	1.3		
RS19-10-C1-4	3.5E-10	0.029	0.258	40.2	2	150	77	0.63	9.03	32.45	0.4	51.4	0.7		
RS19-10-C1-5	1.1E-10	0.016	0.122	26.3	1	118	76	0.66	7.49	19.53	0.4	29.6	0.7	27.9 ± 4.8	45.6 ± 8.4
RS19-10-C2-1	2.0E-10	0.037	0.355	71.1	2	147	68	0.60	9.62	13.38	0.2	22.4	0.3		
RS19-10-C2-2	4.5E-10	0.029	0.389	37.2	2	184	84	0.67	13.34	30.37	0.4	45.7	0.5		
RS19-10-C2-3	4.4E-10	0.038	0.222	29.7	1	183	81	0.69	5.87	40.36	0.6	58.2	0.8		
RS19-10-C2-4	2.6E-10	0.021	0.127	18.9	2	162	81	0.66	6.12	42.93	0.9	65.3	1.4		
RS19-10-C2-5	2.4E-10	0.020	0.175	26.6	1	141	80	0.68	8.96	32.22	0.6	47.4	0.8	/	/
RS17-N4-C1-1A	3.0E-10	0.031	0.142	26.8	1	170	75	0.7	4.6	38.3	0.6	56.8	0.9		
RS17-N4-C1-1	2.8E-10	0.033	0.154	16.4	2	200	92	0.7	4.6	33.2	0.4	45.3	0.5		
RS17-N4-C1-2	8.3E-10	0.074	0.380	65.4	1	250	63	0.6	5.2	41.9	0.4	74.8	0.8		
RS17-N4-C1-3	8.4E-10	0.070	0.613	55.1	1	200	88	0.7	8.7	32.1	0.4	44.1	0.5		
RS17-N4-C1-4	9.7E-10	0.128	0.510	42.9	1	180	113	0.8	4.0	31.9	0.4	41.4	0.5	35.7 ± 7.4	51.6 ± 3.5
RS19-05B-1	4.2E-10	0.054	0.219	45.3	2	146	80	0.65	4.06	32.97	0.5	50.9	0.7		
RS19-05B-2A	1.7E-10	0.021	0.075	18.6	2	170	70	0.63	3.53	36.20	1.1	57.5	1.8		
RS19-05B-3	5.0E-10	0.073	0.265	73.4	1	149	70	0.62	3.64	30.10	0.4	48.5	0.6		
RS19-05B-4	3.1E-10	0.046	0.165	58.3	2	110	72	0.60	3.60	29.58	0.5	49.6	0.8		
RS19-05B-5	3.6E-10	0.036	0.099	26.3	1	180	71	0.64	2.75	49.80	1.2	77.8	1.8	/	/
RS17-N5-1	1.8E-10	0.021	0.087	22.4	2	175	65	0.6	4.1	35.0	0.5	55.1	0.7		
RS17-N5-2	3.0E-10	0.028	0.098	40.7	1	140	60	0.6	3.5	47.1	0.7	79.2	1.1	41.1 ± 6.1	67.1 ± 12.0

Note. a. T——termination; b. L——length; c. W——width; For samples with standard deviation greater than 20%, the mean age is not calculated (Flowers and Kelley, 2011).

Table 3. Results of Zircon (U-Th)/He Analysis

Grain name	^{4}He (cc)	^{238}U (ppm)	^{232}Th (ppm)	eU (ppm)	^{c}T	^{a}L (um)	^{b}W (um)	F(T)	Th/U	Raw age (Ma)	Error (Ma)	Corrected age (Ma)	Error (Ma)	Ave. Raw age and SD (Ma)	Ave. Cor. Age and SD (Ma)
RS17-N1-C4-Z1	2.49E-08	588.88	361.23	673.77	2	200	75	0.74	0.61	106.70	5.95	113.11	8.01		
RS17-N1-C4-Z2	6.92E-09	373.14	424.29	472.85	2	180	65	0.71	1.14	62.66	4.45	88.73	6.31		
RS17-N1-C4-Z3	1.64E-08	1107.38	516.58	1228.78	2	190	53	0.67	0.47	82.73	4.61	97.41	6.90		
RS17-N1-C4-Z4	2.31E-09	217.60	318.86	292.54	2	150	55	0.65	1.47	56.55	4.06	86.41	6.22		
RS17-N1-C4-Z5	1.04E-08	925.97	533.22	1051.27	2	170	50	0.64	0.58	75.55	5.35	117.72	8.35		
RS17-N1-C4-Z6	1.05E-08	980.32	461.13	1088.68	2	130	53	0.64	0.47	87.39	4.88	107.25	7.61		
RS17-N1-C4-Z7	9.86E-09	1249.02	651.77	1402.18	2	130	55	0.65	0.52	58.21	4.12	89.13	6.31	/	/
RS17-N1-C5-Z1	8.15E-09	870.23	767.37	1050.57	2	140	50	0.63	0.88	72.04	5.11	114.90	8.15		
RS17-N1-C5-Z2	2.68E-08	1866.43	1223.56	2153.97	2	150	60	0.68	0.66	74.85	5.29	109.98	7.77		
RS17-N1-C5-Z3	2.38E-08	1596.10	723.78	1766.19	2	190	55	0.67	0.45	76.21	5.38	113.89	8.04		
RS17-N1-C5-Z4	1.04E-08	560.04	398.59	653.71	2	180	55	0.67	0.71	94.72	6.71	142.33	10.08		
RS17-N1-C5-Z5	1.61E-08	847.21	542.20	974.63	2	180	65	0.71	0.64	70.79	5.01	100.01	7.07		
RS17-N1-C5-Z6	2.17E-08	1346.13	755.57	1523.68	2	160	60	0.68	0.56	80.52	5.69	118.61	8.38		
RS17-N1-C5-Z7	8.08E-09	418.03	516.81	539.48	2	150	53	0.64	1.24	117.41	8.36	182.36	12.98	78 ± 9	117 ± 14
RS17-N1-C6-Z1	1.57E-08	1168.61	414.97	1266.13	2	170	53	0.66	0.36	86.17	6.09	131.54	9.29		
RS17-N1-C6-Z2	1.24E-08	1105.77	732.77	1277.97	2	170	50	0.64	0.66	74.17	5.25	115.93	8.20		
RS17-N1-C6-Z3	1.60E-08	1532.07	830.99	1727.35	2	150	50	0.64	0.54	80.08	5.66	125.99	8.90		
RS17-N1-C6-Z4	5.24E-09	440.67	409.93	537.00	2	120	50	0.62	0.93	105.48	7.54	169.78	12.13	86 ± 14	136 ± 24
RS17-N4-C1-Z1	3.83E-09	198.38	185.40	241.95	2	210	59	0.69	0.93	70.34	5.02	102.02	7.28		
RS17-N4-C1-Z2	6.94E-09	198.17	215.01	248.70	2	220	78	0.75	1.08	68.65	4.88	92.01	6.54		
RS17-N4-C1-Z3	1.30E-08	354.01	331.52	431.91	2	280	70	0.73	0.94	71.16	5.04	97.09	6.88		
RS17-N4-C1-Z4	1.16E-08	228.66	211.63	278.39	2	250	95	0.79	0.93	59.94	4.25	75.62	5.36		

RS17-N4-C1-Z5	7.10E-09	293.59	245.53	351.29	2	200	75	0.74	0.84	58.47	4.15	78.81	5.59		
RS17-N4-C1-Z6	1.99E-08	474.62	469.85	585.04	2	260	75	0.75	0.99	75.77	5.37	101.11	7.16		
RS17-N4-C1-Z7	4.35E-09	152.32	162.25	190.45	2	240	70	0.73	1.07	63.24	4.50	86.26	6.14	67 ± 6	90 ± 11

Note. a. L——length; b. W——width; c. T——termination. For samples with standard deviation greater than 20%, the mean age is not calculated (Flowers and Kelley, 2011).

Table 4. Results of Apatite Fission Track Analysis

Sample	No. of Grains .	$^{a}\rho_s$ (10^5/cm^2)	Total $^{b}N_S$	$^{a}\rho_i$ (10^5/cm^2)	Total $^{b}N_i$	$^{a}\rho_d$ (10^5/cm^2)	$^{b}N_d$	$^{c}P(\chi)^2$	$^{d}D_{par}$ (μm)	^{238}U ppm	Central AFT Age (Ma)	±1σ	Pooled AFT Age (Ma)	±1σ	Dis. (%)	MTL c Axis Correction (μm)	SD (μm)	N^e
RS19-05-A	16	5.1	250	32.0	1562	17.7	14503	0.50	1.5	25.3	42.5	5.3	42.5	2.9	0	13.5	1.4	8
RS19-05-B	20	7.4	368	31.1	1556	16.1	14503	0.02	1.5	28.4	57.1	4.4	57.1	3.3	20	13.96	1.2	27
RS19-08	17	3.1	263	17.8	1488	18.8	14503	0.60	1.6	14.9	50.0	3.3	49.0	3.3	0	14.33	1.1	9
RS19-07	12	5.4	209	25.5	990	18.1	14503	0.17	1.6	23.6	56.9	7.7	57.2	4.4	11	13.41	1.3	15
RS17-N5*	22	5.2	179	-	-	-	-	0.00	1.1	2.1	89.0	10	96.8	7.3	37	12.48	1.3	5
RS19-10-C1	20	5.7	196	23.5	810	18.4	14503	0.43	1.5	17.4	67.0	5.3	67.0	5.3	0	13.44	1.2	4
RS17-N4-C1*	14	4.8	174	-	-	-	-	0.09	1.4	3.8	51.3	4.8	51.3	3.9	19	12.29	0.5	2
RS19-06-C3	12	2.1	93	15.8	697	16.5	14503	0.23	1.6	15.8	33.0	4.1	33.1	3.7	18	-	-	0
RS19-06-C4	20	2.0	189	14.2	1317	14.5	14503	0.10	1.5	13.5	31.2	2.9	31.3	2.4	19	13.24	0.6	3
RS19-06-C6	20	2.0	170	15.6	1313	17.3	14503	0.10	1.6	12.9	33.4	3.4	33.6	2.7	24	14.45	1.0	3
RS17-N1-C6*	20	2.0	124	-	-	-	-	0.69	1.3	2.2	33.6	3.0	33.6	3.0	0	-	-	0
RS17-N1-C4*	18	3.4	129	-	-	-	-	0.00	1.2	2.3	62.0	10.0	71.0	6.3	56	12.70	0.2	3
RS17-N1-C5*	9	4.5	57	-	-	-	-	0.03	1.2	4.8	77.0	15.0	77.0	10	39	-	-	0
RS17-N1-C1	26	5.4	313	19.8	1143	12.5	8790	0.04	1.7	23.5	53.1	4.3	51.7	10.8	22	13.30	0.6	6
RS17-N1-C2	11	4.6	69	17.5	262	12.4	8790	0.89	1.8	20.6	49.7	6.7	49.3	10.3	0	12.26	1.0	5
RS17-N1-C3	20	13.6	481	30.8	1091	12.2	8790	0.00	2.0	36.1	83.0	10.0	81.0	16.9	47	12.78	1.5	15

*Concentration of U measured by LA-ICP-MS

a. $\rho_{(i,s,d)}$ are track density of induced, spontaneous, dosimeter tracks.

b. Ni, Ns, and Nd are the number of induced, spontaneous, and dosimeter tracks counted.

c. P(χ)2 value of the chi-square age homogeneity test.

d. Dpar measurements are etch pit diameters used as a proxy for the influence of chemical composition on track annealing [Donelick et al., 2005]. Three to five Dpar measurements were used for each grain.

e. The number of confined tracks